Manuscript Number:

Title: Effect of water depth, and the bottom boundary layer upon internal wave generation over abrupt topography

Article Type: Original Papers

Keywords: internal waves, bottom boundary layer, topography

Corresponding Author: Dr. Jiuxing Xing, Ph.D.

Corresponding Author's Institution:

First Author: Jiuxing Xing, Ph.D.

Order of Authors: Jiuxing Xing, Ph.D.; Alan M Davies

Abstract: The role of water depth, and bottom boundary layer turbulence upon lee wave generation in sill regions is examined. Their effect upon vertical mixing is also considered. Calculations are performed using a non-hydrostatic model in cross-section form with a specified tidal forcing. Initial calculations in deeper water, and a sill height such that the sill top is well removed from the surrounding bed region, showed that downstream lee wave generation, and associated mixing increased as bottom friction coefficient k increased. This was associated with an increase in current shear across the sill. However, for a given k, increasing vertical eddy viscosity Av reduced vertical shear in the across sill velocity, leading to a reduction in lee wave amplitude and associated mixing. Subsequent calculations using shallower water, showed that for a given k and Av lee wave generation was reduced due to the shallower water depth and changes in the bottom boundary layer. However in this case (unlike in the deep water case) there is an appreciable bottom current. This gives rise to bottom mixing which in shallow water extends to mid-depth and enhances the mid-water mixing that is found on the lee side of the sill. Final calculations with deeper water, but small sill height showed that lee waves could propagate over the sill, thereby reducing their contribution to mixing. In this case bottom mixing was the major source of mixing which was mainly confined to the near bed region, with little mid-water mixing.

Effect of water depth, and the bottom boundary layer upon internal wave generation over abrupt topography

by

Jiuxing Xing and Alan M. Davies
Proudman Oceanographic Laboratory
6 Brownlow Street
Liverpool, UK, L3 5DA

ABSTRACT

The role of water depth, and bottom boundary layer turbulence upon lee wave generation in sill regions is examined. Their effect upon vertical mixing is also considered. Calculations are performed using a non-hydrostatic model in cross-section form with a specified tidal forcing. Initial calculations in deeper water, and a sill height such that the sill top is well removed from the surrounding bed region, showed that downstream lee wave generation, and associated mixing increased as bottom friction coefficient k increased. This was associated with an increase in current shear across the sill. However, for a given k, increasing vertical eddy viscosity A_v reduced vertical shear in the across sill velocity, leading to a reduction in lee wave amplitude and associated mixing. Subsequent calculations using shallower water, showed that for a given k and A_v lee wave generation was reduced due to the shallower water depth and changes in the bottom boundary layer. However in this case (unlike in the deep water case) there is an appreciable bottom current. This gives rise to bottom mixing which in shallow water extends to mid-depth and enhances the mid-water mixing that is found on the lee side of the sill. Final calculations with deeper water, but small sill height showed that lee waves could propagate over the sill, thereby reducing their contribution to mixing. In this case bottom mixing was the major source of mixing which was mainly confined to the near bed region, with little mid-water mixing.

1. INTRODUCTION

One of the major problems in physical oceanography is how energy of meteorological and tidal origin is transformed through the internal wave field (Van Haren, 2004) into small scale mixing processes and how this mixing influences the large scale circulation (e.g. Samelson 1998, Spall 2001, Saenko and Merrifield 2005, Saenko 2006). In terms of wind forcing, recent calculations have shown that vorticity associated with small scale eddies in the ocean can significantly influence the downward diffusion of the wind's momentum and hence mixing at depth (Zhai et al 2005). In shallow seas, wind forcing in the regions of surface and bottom fronts gives rise to internal waves which can be trapped in the frontal region, or propagate away (Davies and Xing 2004, Xing and Davies 2005). In the case of internal waves propagating along the thermocline there can be appreciable mixing at the level of the thermocline, namely "internal mixing" (Van Haren and Howarth 2004), that can lead to enhanced across thermocline exchange (Rippeth et al 2005) and breakdown. In shallow sea areas the existence of cold water bottom domes provides a mechanism for internal wave trapping and associated mixing with changes in circulation (Davies and Xing 2005, Xing and Davies 2006a).

In shelf edge regions where the thermocline intersects the shelf slope, the on-off-shelf motion of the tide gives rise to an internal tide which propagates into the ocean (see Baines 1995, Vlasenko and Stashchuk, 2006, Vlasenko et al 2005, for a comprehensive review). However the energy dissipation and mixing due to wave-wave interaction associated with this radiating tide is thought to be small. However, recently it has been suggested that internal mixing of tidal origin occurs in regions of rough topography (e.g. Xing and Davies 2006b,c) due to its interaction with small scale topography. Consequently in the last few years significant modelling and measurements have been made at oceanic features e.g. rides, seamounts and shelf slopes (Legg and Adcroft 2003, Legg 2004a,b, Hosegood and Van

Haren (2004), New and Pingree (1990), Van Haren (2004), Legg (2004a,b), Dewey et al (2005), Gerkema and Zimmerman (1995), Gerkema (2001, 2002), Gillibrand and Amundrud (2007), Jeans and Sherwin (2001a,b) where there is appreciable small scale topography. However using models to examine the energy cascade in such areas is particularly difficult due to the lack of detailed measurements of far field effects along the extensive open boundaries surrounding these features. This suggests that detailed measurements and associated modelling in semi-enclosed regions with abrupt topography and strong tidal currents e.g. sills in fjords and lochs (e.g. Inall et al., 2004, 2005) could yield insight into the role of small scale topography upon internal tidal mixing.

In terms of tidal mixing and dissipation this is particularly large on continental shelves. In these regions, strong tidal currents flowing over a rough sea bed produce a thick (of order 50 m) turbulent bottom boundary layer. In many regions e.g. shallow (water depth below 50 m) areas of the European Continental Shelf, the bottom boundary layer thickness exceeds the water depth and the water column remains well mixed. In this case the mixing is termed “external mixing” in that it is produced at the bottom of the water column and diffuses away from the bottom boundary layer into the water column. The intensity and vertical extent of this turbulent boundary layer depends on tidal current strength and bottom roughness.

In deeper water or regions of weak tidal currents, the bottom turbulent boundary layer only occupies a small fraction of the water column (e.g. Davies and Jones 1990) and in summer time a thermocline forms at depth below a well mixed surface layer. The position of the thermocline and the associated circulation field are determined by the balance between turbulence generation and buoyancy suppression (e.g. Xing and Davies 2001).

In regions such as banks or sills at the entrance to lochs or fjords where the topography is rough and changes rapidly on space scales comparable to the tidal excursion recent measurements (Inall et al 2004, 2005) suggest that there is appreciable mixing of tidal origin within the thermocline, namely “internal mixing”. The small geographical extent of these regions, and particularly in the case of lochs and fjords the fact that tidal forcing is through one small open boundary, makes them ideal for modelling studies. In addition detailed measurements of tidal forcing and mixing can be performed. However, as we will show here, besides detailed measurements of tidal forcing and resulting mixing, significant additional measurements are required, particularly bed roughness and turbulence over the sill and in the bottom boundary layer downstream of the sill, in order to close the problem to such an extent that rigorous model validation is possible.

Recent measurements in Loch Etive (Inall et al 2004, 2005) and associated modelling studies showed that a non-hydrostatic model in cross sectional form, with idealized topography, could reproduce the major features of the hydraulic transition, lee wave production, and mixing found in the observations (Xing and Davies 2006a, hereafter XD06). In addition the model demonstrated the importance of small scale topography on the leeside of the sill, upon “internal mixing” of tidal origin (XD06). In subsequent calculations Davies and Xing 2007, hereafter DX07 the importance of stratification and its vertical variation upon lee wave generation and mixing was examined. These calculations showed that the value of the buoyancy frequency in the region of the top of the sill was critical in determining the extent of lee wave generation (DX07). In this paper that work is extended to examine the role of bottom friction effects and the thickness of the turbulent bottom boundary layer of tidal origin upon lee wave formation and associated mixing in the region of sills.

The model is identical to that used previously (XD06) and is briefly described in the next section. Subsequently (Section 3) results are presented to show the influence of bottom friction and vertical eddy viscosity, which control turbulence in the bottom boundary layer, upon lee wave generation and mixing in the region of abrupt topography. These calculations are extended in Section 4, to examine the effect upon lee waves and mixing of water depth change. In particular for the case of a shallow region where the bottom boundary layer thickness is comparable to the height of the sill or bank. A final section summarized the major findings of the study, and the extent and comprehensive nature of data sets required for model validation purposes.

2. NUMERICAL MODEL

As this paper is mainly concerned with how sill depth, aspect ratio and the tidally generated bottom turbulent boundary layer influence mixing in sill regions, idealized sill topography was used in all calculations. In addition a two dimensional (x, z) cross sectional form of the model was applied, although this means that along sill and across channel changes in topography were excluded. Consequently horizontal gyres that can be produced by along sill topography or in the region of a bank cannot occur. However, such effects are outside the scope of this paper where the emphasis is the role played by the bottom turbulent boundary layer. Here a simple symmetric form of sill topography and water depths approximating those of Loch Etive where recent measurements were made (Inall et al 2004, 2005) is used (Fig. 1a,b). Initially calculations were performed with a sill in a water depth h = 100 m (Fig. 1a) although subsequently water was shallowed to h = 50 m. By varying the sill half width (a_s), the vertical eddy viscosity (A_V) due to tidal mixing, together with water depth and sill height (Table 1), the influence of these parameters that control the bottom boundary layer, upon flow field, internal wave spectra and mixing could be determined.

As shown by XD07 the vertical velocity and the presence of a hydraulic transition in the sill region means that the hydrostatic approximation is not valid and non-hydrostatic effects must be taken into account. Following previous modelling in sill regions (XD06) the MIT model (Adcroft et al., 1997 Marshall et al 1997a,b) which is based on a z coordinate in the vertical and a finite volume discretization was used. However other non-hydrostatic models using sigma coordinates exist in the literature (e.g. Berntsen et al (2006)) and give comparable solutions for non-hydrostatic problems.

Topography in the sill region (Fig. 1) is characterized by a constant depth domain (water depth h = 100 m or 50 m (Table 1)) on either side of the sill, with an open mouth at x = -80 km, where M_2 barotropic tidal forcing is applied. The sill is situated at x = 0, with a water depth (sill depth h_s) above the sill that was varied in the calculations. Water depths increasing to h = 100 m or 50 m fixed in all calculations on both sides of the sill, with a closed boundary at its eastern end (x = 80 km). Initial conditions consisted of a horizontal uniform temperature field, with a vertical temperature gradient that was the same in all calculations, namely a buoyancy frequency (N) = 0.01 s^{-1}. The Coriolis parameter f was fixed at 1.2 x 10^{-4} s^{-1}, typical of northern latitude regions where fjord systems occur (Stiegbrandt 1999). Also at time t = 0, zero horizontal (u) and vertical (w) velocity were specified. A fine uniform grid resolution dz = 1 m was used in the vertical with the horizontal grid gradually varying from dx = 10 m in the sill region to 100 m outside this area. With such a fine grid the background coefficient of horizontal viscosity was set at $A_h = 10^{-1}$ m^2 s^{-1}. Similarly small background diffusivities of $K_V = K_h = 10^{-7}$ m^2 s^{-1} were used in the calculations. However, the vertical eddy viscosity, assumed to be of tidal origin was varied between calculations (see Table 1) in order to determine its influence on bottom boundary thickness and hence lee wave generation and mixing, as identified by R_i number distributions. Consequently mixing was mainly controlled by small scale processes that could be resolved on the grid, and high mixing regions identified by low Richardson number values.

At sea surface and sea bed, a no flux boundary condition was applied together with a zero surface stress condition and quadratic friction at the bed. A time step dt = 2s, was used in all calculations. At the western open boundary barotropic tidal forcing corresponding to an external M_2 tide was applied of the form

$$U = F(t)U_o \cos \omega t$$

Where U_o is tidal amplitude and ω its period with F(t) increases exponentially from 0 to 1 at t greater that 0.25 of an M_2 tidal period. By this means tidal forcing was gradually increased at the open boundary.

3. NUMERICAL CALCULATIONS

3.1 Narrow Sill Calculations

(a) $k = 0.0025$, $A_v = 0.001$ m^2 s^{-1}

In an initial calculation (Calc 1, Table 1) the water depth h = 100 m, with sill depth h_s = 15 m, and hence sill height h_o = 85 m. The sill half width a_s = 500 m. The initial vertical variation of temperature is as shown in Fig. 1a, giving a constant buoyancy frequency N = 0.01 s^{-1}. The value of bottom friction coefficient k = 0.0025, with K_v, A_h, K_h values as given in Section 2, and A_v = 0.001 m^2 s^{-1} (Table 1). These parameters are typical of sill regions and were used in the Loch Etive calculations (XD06) where they yielded results in good agreement with observations (Inall et al., 2004, 2005). In all calculations the model started from a state of rest with horizontal isotherms and a vertical temperature gradient (Fig. 1a). Tidal forcing was introduced through the left open boundary with U_o = 0.15 m s^{-1}. The right hand boundary (head of the loch) was closed. As a detailed description of tidal flow over sills and small scale topography is given in XD06, with an intercomparison with appropriate observations (Inall et al., 2005, 2006), only the major features are presented here, at the end of the first cycle (Fig. 2a) and second cycle (Fig. 2b).

Initially tidal flow through the left open boundary causes isotherms to rise on the left hand side of the sill. Based on the water depth away from the sill, h = 100 m, maximum input tidal velocity U_o = 0.15 m s^{-1}, and buoyancy frequency N = 0.01 s^{-1}, the Froude number away from the sill, $F_r = U_o/hN = 0.15$ is sub-critical (namely $F_r < 1$). However, as the water over the sill accelerates, by t = 8/8T (where T is a tidal cycle) it reaches a sill velocity U_s =

0.35 m s^{-1} (Fig. 2a). Also the sill water depth is 15 m, giving a sill Froude number $F_s = U_s/h_sN = 2.3$, namely a super-critical flow. However, on right side of the sill, the water is at rest and the flow is sub-critical. Hence a hydraulic transition occurs on the lee side of the sill with an associated downwelling of the isotherms. This gives rise to the production of a temperature gradient with associated internal waves (Fig. 2a). At the end of the first tidal cycle, namely t = 8/8T, the initial hydraulic transition has been advected downstream by the flow.

Vertical velocity contours on the leeside of the sill at this time show the presence of lee waves, with wavelengths of order 100 m. This wavelength is comparable to those observed on the lee side of sills with similar topography (see Inall et al., 2004, 2005) and found in models of sill regions (e.g. XD06, DX07, Vlasenko et al 2005). Associated with the lee waves are regions of enhanced/reduced u velocity, giving rise to an increase/decrease in the U velocity on the lee side of the sill as shown in Fig. 2a. During flood tide, the lee waves are trapped on the lee side of the topography and their amplitude increases. Associated with the lee waves, and the current jet that separates from the top of the sill (Fig. 2a), are regions of convective overturning and shear induced mixing giving rise to negative Richardson numbers, and values below the critical Richardson number $R_{ic} = 0.25$ (Fig. 2c). In these regions there is significant vertical mixing as shown by the isotherms (Fig. 2c). As tidal velocity decreases lee waves that were trapped on the leeside of the topography propagate towards the sill, but in the case of a shallow sill they cannot propagate over it, and energy is lost due to enhanced mixing on the lee side of the topography. A detailed discussion of this is beyond the scope of the present paper, but given in XD06. However, the main features of the across sill flow can be appreciated from the time series at x = 0 (centre of the sill) given in Fig. 3a.

Time series of temperature and velocity profiles from x = 0 show (Fig. 3a) the velocity increasing during the “ramp-up” stage (up to t = 0.25T). This produces an upwelling of isotherms on the top of the sill with an associated decrease in temperature in the near bed region. As the tide reverses the hydraulic transition formed on the lee side of the sill is advected back over the sill producing the rapid temperature change at about t = 0.3T (Fig. 3a). The symmetric nature of the topography means that a corresponding hydraulic transition is formed on the left hand side, and is also advected by the flow. It is evident from Fig. 3a, that a periodic flow dominated by the M_2 period, although with some higher harmonic, as shown by the two maxima/minima per tidal cycle, is rapidly established after the first tidal cycle. Although there is no evidence of lee wave advection or propagation onto the sill, time series of temperature, u and w- velocity at x = 500m, show a significant lee wave signal on the lee side of the sill as the tide floods (Fig. 3b).

As time progresses, lee waves on the lee side of the sill give rise to some mixing in this region (Fig. 2b) (although some of this can be due to the intrusion of water advected over the sill) producing a reduction in the intensity of the hydraulic transition. Consequently the sharpness and form of the hydraulic transition is reduced with time as shown by the time series of the temperature field in Fig. 3a, as a progressively more diffuse temperature front formed in the lee of the topography is advected over the sill.

After two tidal cycles (t = 16/8T) the vertical and horizontal extent of the well mixed region on the lee side of the topography has increased. In addition the upper water column stratification down stream of the hydraulic transition has weakened. The reduction in stratification on the lee side of the topography that occurred during the first tidal cycle, means that the buoyancy frequency in the sill region (N_s) has changed giving rise to an increase in lee wave magnitude as shown by the vertical velocity contours (Fig. 2b). As the influence of buoyancy frequency on the lee side of topography is discussed in detail in DX07 it is not considered here. However, the extent to which changes in k and A_v influence the mixing and hence the spectrum of the internal tide and lee waves is examined here and quantified in terms of the depth integrated power spectrum of the vertical velocity after 8 tidal cycles (Fig. 4a).

It is evident from Fig. 4a, that the power spectrum exhibits distinct peaks at the M_2, M_4, M_6 and M_8 frequencies, showing that a significant M_2 internal tide has been generated, with non-linear effects producing higher tidal harmonics. In addition there is a peak at the high frequency end of the spectrum, namely at a period of about 12 mins, which is characteristic of lee waves generated over topography of the scale used here with a buoyancy frequency $N_s = 0.01\ s^{-1}$. Based on simple theory for $N_s = 0.01\ s^{-1}$, a lee wave period of about $2\pi/N_s = 10$ mins would be expected. This is close to that found in the model, which takes account of mixing in the sill region and hence a change in N. Above the lee wave frequency, energy decreases as frequency increases.

(b) k = 0.025, $A_v = 0.001 m^2\ s^{-1}$

In order to examine the influence of bottom friction and hence stress at the bottom of the turbulent bottom boundary layer, upon lee wave formation, mixing and internal wave spectrum, the previous calculation was repeated with k = 0.025 (Calc 2). Increasing the bottom drag coefficient, leads to a reduction in bottom current on top of the sill, although there is a slight increase in the surface current (compare u current contours at t = 8/8T in Figs. 2a and 5a). Although this change in current profile and magnitude is small, it does influence the intensity of the hydraulic transition on the lee side of the sill and hence the mixing in this region. This is clearly evident in the differences in isotherm and R_i number distributions between Calcs 1 and 2 (compare Figs. 2c and 5c). It is evident from Figs. 2c and 5c that the vertical extent of the well mixed region has been reduced, although its lateral extent is increased by this increase in k. This is associated with the increase in lee wave intensity and downstream extent, together with the u component of current due to this increase in k.

As discussed in connection with Calc 1, changes in mixing and hence N on the lee side of the topography, influences lee wave production in such regions and hence subsequent mixing. Consequently this short term change in mixing accumulates in the longer term, and is clearly evident in the differences in isotherm distributions at t = 16/8T (compare Figs. 2b and 5b).

Although the power spectrum for the two cases (Figs. 4a and 4b) show similar distributions of energy across the frequency band, a detailed examination suggested that the energy in the lee wave band had increased, with an associated reduction in the tidal band, as k had increased. Additional calculations (not presented) showed that as k decreased so did energy in the lee wave band, although the dominant features of the spectrum were consistent with those shown in Figs. 4a,b.

(c) k = 0.0025, $A_v = 0.005$ m^2 s^{-1} (Calc 3)

To examine the influence of vertical eddy viscosity, and hence enhanced turbulence in the near bed region, Calc 1 was repeated with A_v increased to $A_v = 0.005$ m^2 s^{-1} (Calc 3). This increase in A_v is assumed to arise through an increase in tidal turbulence produced by a rougher sea bed in the sill region. Measurements (Moum and Nash, 2000) suggest that bed roughness with associated enhanced turbulence arise in sill regions due to the stronger currents over the sill crest. As in Calcs 1 and 2, a hydraulic transition develops on the lee side of the topography (Fig. 6a) although the intensity and downstream extent of the mixing are significantly reduced compared to Calcs 1 and 2, compare Figs 2a, 5a and 6a. This is due to a reduction in lee wave intensity as shown by the reduction in magnitude of the vertical velocity associated with the lee waves (see Figs 2a and 6a). The associated reduction in mixing due to decreased lee wave activity means that the buoyancy frequency in the region of the sill is maintained close to its initial value, unlike in Calc 1 where lee wave intensity and mixing increase with time. Consequently at t = 16/8T the mixed region (not shown) is substantially less than found at this time in Calc 1. The reduction in mixing between the present calculation and Calc 1, is evident in the reduced intensity and lateral extent of the region where R_i is below its critical value of 0.25 (compare Figs. 6b and 2c).

Time series of temperature and velocity from the centre of the sill (Fig. 6c) over the first two tidal cycles, show similar current magnitude and time variations to those found with $A_v = 0.001\ m^2\ s^{-1}$. However, the effect of increasing A_v has been to slightly reduce vertical shear particularly in the near bed region, although there is no significant change in across sill velocity and hence sill Froude number F_s. Despite the fact that F_s is the same in both calculations, it is apparent from the temperature time series at x = 0 (compare Figs. 3a and 6c) that after the "spin up" period there has been appreciably more mixing in Calc 1, than the present calculation. As discussed previously this mixing is associated with lee waves generated on the lee side of the sill. Differences in the intensity of these lee waves and the associated level of mixing is evident from the comparison of time series at x = 500 m (Figs. 3b and 6d) that show a significant reduction in lee wave intensity when A_v is increased.

Although Fig. 6d shows that the magnitude of the lee waves at x = 500 m has been reduced, the power spectra (Fig. 4c) reveals that besides this reduction across the lee wave band, the distribution of energy across the band has changed (compare Figs. 4a and 4c). In essence because the mixing has been reduced, the buoyancy frequency has remained more constant in time and energy has been retained (although reduced) at the dominant lee wave frequency (determined by buoyancy frequency, for fixed topography and forcing frequency) (Fig. 4c) rather than spread over the band (Fig. 4a). The change in mixing in the sill region as to be expected also influences the energy in the internal tide at this location. Since the intensity and location of internal tide generation along a slope, together with its propagation away from its generation point changes with buoyancy frequency (for a given topography, forcing and Coriolis frequency) then changes in mixing will also affect the low frequency internal tide end of the spectrum.

(d) $k = 0.0025$, $A_v = 0.01$ m^2 s^{-1} (Calc 4)

Increasing A_v to $A_v = 0.01$ m^2 s^{-1} significantly reduces the magnitude of the hydraulic transition and the downstream extent of the well mixed region (Fig. 7a). The magnitude of the maximum across sill velocity is slightly reduced by about 5 cm s^{-1} (Figs. 7a,b), although the sill Froude number remains supercritical ($F_s = 2$). Contours of w (not presented) show weak lee waves close to the topography on its downstream side. Time series of temperature and velocity from $x = 0$ (Fig. 7b) show that the effect of further increasing the vertical eddy viscosity compared with previously is to slightly reduce the shear in the bottom boundary layer, with the current exhibiting a near linear decrease from surface to bed.

However, the magnitude of the current above this layer is not significantly affected nor is its time variation. Consequently as discussed previously, F_s is supercritical and a hydraulic transition is formed and advected across the sill (Fig. 7b). Unlike previously (Calc 1) the absence of significant lee waves downstream of the sill means that there is little mixing in this region. Consequently the generation and advection of the temperature front is a persistent feature of the tidal flow over the sill and a clear indicator of the absence of lee wave mixing.

Comparing power spectra at $x = 500$ m from this calculation (Calc 4) (Fig. 4d, $A_v = 0.01$ m^2 s^{-1}) with earlier calculations (Fig. 4a, $A_v = 0.001$ m^2 s^{-1}) and Fig. 4c ($A_v = 0.005$ m^2 s^{-1}), it is clearly evident that energy at the high frequency end of the spectrum has been significantly reduced due to this additional increase in A_v. In addition internal tide generation has been suppressed, as indicated by the lack of peaks at the low frequency end of the spectrum.

This series of calculations shows that the value of vertical eddy viscosity and hence turbulence in the tidal bottom boundary layer has a significant influence upon lee wave generation and hence mixing on the lee side of shallow topographic features. In reality tidal turbulence (and hence tidally induced viscosity) depends on tidal velocity and bed roughness. Consequently in shallow regions such as sills it is appreciable and will play a role in determining the intensity of lee wave generation and associated mixing.

4. INFLUENCE OF WATER DEPTH

In this calculation (Calc 5) the water depth outside the sill region was reduced to 50 m (Fig. 1b). This value was chosen because it corresponded to the depth at which the flow in previous calculations was non-zero. Hence bottom frictional effects away from the top of the sill, which were previously zero, are now non-zero. In addition to maintain the same sill profile near its top and identical stratification in this region, the initial conditions were as previously, but with the sea bed now at z = -50 m (Fig. 1b). In order to maintain the same sill Froude number, the amplitude of the forcing velocity was reduced to 0.18 m s^{-1}, a value that gave an across sill flow comparable to that used earlier.

(a) $k = 0.0025, A_v = 0.001\ m^2\ s^{-1}, h = 50\ m$ *(Calc 5)*

In an initial calculation (Calc 5) with h = 50 m, values of k and A_v were as in Calc 1. Contours of u current velocity in the sill region at t = 8/8T show (Fig. 8a) an across sill flow comparable to that found in Calc 1 (Fig. 2a) and hence the same sill Froude number F_s. However, the temperature contours (Fig. 8a) at this time do not show the presence of the sharp surface frontal feature found previously (Fig. 2a) at x = 800 m. A well mixed region and some convective overturning does exist on the lee side of the sill (Fig. 8a) although this is appreciably less than previously (Fig. 2a). Contours of vertical velocity (not presented) reveal very little lee wave activity in the region at this time, unlike previously (Fig. 2a) and hence away from the sill area, the u velocity shows a uniform variation with no indication of patches of enhanced velocity as found in Calc 1 (Fig. 2a) due to lee wave activity. However, subsequently (Fig 8b) some lee wave does develop at t=16/8T (see later discussion).

The R_i number and isotherm distribution at t = 8/8T (Fig. 8c) show a region of critical R_i number in the lee of the sill from about z = -15m to -40 m extending downstream to beyond x = 1000 m. This is comparable to that found previously (Fig. 2c), although the isotherms show the absence of lee waves. This suggests that early in the calculation (first tidal cycle) mixing is produced by the flow over the sill, rather than the lee waves that are generated in the deep water case. Also in this shallow water case there is some indication of bottom mixing close to the sill.

After two tidal cycles (t = 16/8T) (Fig. 8d) there is clear evidence of bottom mixing as shown by the presence of two bed regions of critical R_i number, which are independent of the critical R_i number, higher in the water column. Such separate areas were not found in the deep water calculations (Fig. 2d). As time progresses, bottom generated turbulence and mixing increases, and in the region of the sill it extends into the mid-depth part of the water column (not shown).

Time series of temperature and velocity at x = 0 (the top of the sill) shows (Fig. 9a) that during the spin up period, (namely to t = 0.25T) comparable velocities and displacements of the isotherms to those found previously occur (compare Figs. 3a and 9a). However, after the first tidal cycle, when some lee waves are generated downstream of the sill as shown in the time series at x = 500 m (Fig. 9b), the across sill temperature and velocity time series is appreciably different from the deeper water case (compare Figs. 3a and 9a). The reason for this is that the duration and magnitude of the lee waves generated in the shallow case (Fig. 9b) is appreciably less than when h = 100 m (Fig. 3b).

Differences in the level of mixing and lee wave intensity between shallow and deeper water cases is evident from a comparison of Figs. 8b and 2b. Although the sill depth h_s

across sill velocity and sill Froude number F_s are the same with h = 50 m and 100 m, it is apparent that lee wave generation and associated mixing that occurs on the lee side of the sill when h = 50 m (Fig. 8b), is appreciably less than when h = 100 m. This suggests that the closer proximity of the sea bed to the top of the sill where the lee waves are generated, reduces the amplitude of the lee wave. This is confirmed by comparing power spectra from the h = 50 m calculation (Fig. 4e) with that determined with h = 100 m (Fig. 4a). Although the low frequency end of the power spectrum are comparable; showing the presence of the M_2 internal tide and its higher harmonics, it is evident that there is no appreciable increase in power at the high frequency end, corresponding to the generation of strong lee waves as found previously when h = 100 m (compare Figs. 4a and 4e). This suggests that the decrease in water depth and the proximity of the top of the sill to the viscous bottom boundary layer significantly reduces lee wave generation and any associated mixing.

(b) *$k = 0.0025$, $A_v = 0.01\ m^2\ s^{-1}$, $h = 50\ m$ (Calc 6)*

To examine to what extent increasing vertical eddy viscosity to $A_v = 0.01$ m^2 s^{-1} in the shallow water case influences lee wave generation and mixing, the previous calculation was repeated with this high A_v value (Calc 6). After the first tidal cycle, the distribution of isotherms and u currents (not presented) showed a small hydraulic transition on the lee side of the sill with a reduced level of mixing compared to $A_v = 0.001$ m^2 s^{-1} (Fig. 8a). Vertical velocity contours (not presented) revealed a small lee wave signal downstream of the sill.

The mixed water region on the lee side of the sill increased with time (t = 16/8T, Fig. 10a), although its downstream extent was reduced compared to previously (compare Figs. 10a and 8b). This was due to the decrease in lee wave intensity and the lateral extent of the downstream region of significant lee wave activity (Fig. 10a). This resulted in reduced mixing due to lee waves in the downstream region because of the increase in A_v, although the regions of bottom and mid-water mixing close to the sill were no longer separate (compare

Figs. 8d and 10b). In essence as eddy viscosity is increased, the thickness of the bottom turbulent Ekman layer is increased to such an extent that it overlaps the turbulent mid-water region. The reduction in mid-water mixing due to the decrease in lee wave activity is confirmed by the time series of the isotherm distribution on the top of the sill (Fig. 10c). Comparison with Fig. 9a, clearly shows that although the time series are comparable during the "spin up" period, the broadening in time of the hydraulic transition and the vertical weakening of the temperature gradient that occurs with $A_v = 0.001\ m^2\ s^{-1}$, does not arise when $A_v = 0.01\ m^2\ s^{-1}$. This result is comparable to that found in the deeper water case with $A_v = 0.01\ m^2\ s^{-1}$, where the computed time series on top of the sill (Fig. 7b) shows similar features to that shown in Fig. 10c. As in the deep water case, increasing A_v from $0.001\ m^2\ s^{-1}$ to $0.01\ m^2\ s^{-1}$, leads to a reduction in energy in the high frequency lee wave band of the spectrum (compare Figs. 4e and 4f). This confirms that irrespective of water depth, the value of A_v controls lee wave formation and the associated mixing.

(c) $k = 0.0025$, $A_v = 0.001\ m^2\ s^{-1}$, $h_o = 20$ m, $h = 100$ m (Calc 7)

From the previous calculations it is evident that both A_v values and proximity of the sill top to the near bed region controls lee wave generation and associated mixing. To determine to what extent total water depth influences the solution when the sill top is close to the near bed region and hence the turbulent bottom boundary layer, Calc 5 was repeated with $h_o = 20$ m, namely a small sill height close to the bed, but in a water depth of 100 m, hence $h_s = 80$ m.

To be consistent with Calc 5, and enable across sill flows to be compared when water depth changes from 50 m to 100 m, the input forcing was adjusted so that the maximum across sill velocity was comparable to that found in Calc 5 (namely $0.5\ m\ s^{-1}$). Although the Froude number away from the sill F_r was comparable to that used previously, the increase in h_s while maintaining U_s led to a decrease in F_s. However, despite this lower value of F_s, significant lee waves were formed on the lee side of the sill as shown by the vertical velocity contours at t = 8/8T (Fig. 11a). This is in marked contrast to the lee wave distribution found in Calc 5, where the water depth was only 50 m. However, despite the larger lee wave signal at this time there does not appear to be significant overturning and mixing in the water column compared to Calc 5 (compare isotherms in Figs. 8a and 11a). In the present calculation mixing is mainly confined to the near bed region, as shown by the R_i number distribution (Fig. 11b).

The increase in sill water depth means that lee waves and internal tides in the present calculation can propagate over the sill whereas in previous calculations the vertical velocity over the sill was zero. The time series of vertical velocity at x = 0 (centre of sill) clearly shows (Fig. 12) a significant lee wave signal (period of order 12 mins) and internal tidal signal (period of order 12 hours). These periods are also present in the time series of isotherms and u-components of current. Both the isotherms and u-currents show similar longer (of order hours) term variations to those found in the shallower water case (compare Figs. 12 and 9a), with comparable maximum surface tidal velocities. However, in the present calculation there is a significant lee-wave signal as the tide reverses due to lee waves being advected over the sill. The advection of lee waves over the sill due to its increased depth compared to previously means that they do not break and contribute to mixing in the sill region. However since they are generated close to the seabed (due to the small height of the topography) means that they are dissipated close to their generation point by bottom frictional effects. This leads to enhanced bottom mixing intensity downstream of the sill, compared to the higher sill case (compare Figs. 2c and 11b).

In previous calculations (Calcs 1 to 6), the sill depth h_s = 15 m, was so shallow that propagation or advection of internal waves over the sill could not occur. Consequently the vertical velocity on the sill top was zero. In the present case with a deep sill the depth integrated spectrum of the vertical velocity (Fig. 13a) based on the eight tidal cycle, showed spikes at the M_4, M_8 and M_{16} signal, although there were dips at the M_2, M_6 and M_{12} frequency. This suggests that non-linear effects associated with such small scale topography primarily produce higher harmonics of the tide close to the sill, which in the case of deep water above the sill can propagate over it. Certainly in the case of a shallow sill h_s = 15 m, no internal waves occurred on the top of the sill. However, a detailed study of the influence of sill depth h_s upon internal wave propagation is beyond the scope of the present paper.

Although there is some energy at the lee wave frequency at the high frequency end of the spectrum, there is no distinct peak (Fig. 13a). Similarly at x = 500 m the high frequency end of the spectrum shows (Fig. 13b) a rapid fall off with frequency comparable to that found with h = 50 m (Fig. 4d). However in the deeper water case there is increased energy at the low frequency (tidal band) of the spectrum.

These calculations suggest that when the top of the sill is close to the sea bed region, there is substantial mixing in the bottom boundary layer. Increases in turbulence (A_v) and bottom friction in this region, giving a thicker turbulent bottom boundary layer, dissipate the lee waves that are generated on the lee side of the sill. In the case of shallow water depths where the turbulent boundary layer can extend close to the sea surface (e.g. h = 50 m) the water on the lee side of the sill experiences enhanced mixing. As water depth increases although sill height h_o remains small mixing in the bottom boundary layer is isolated from the main part of the water column, that remains stratified. The effect of increasing water depth also means that for a fixed h_o, sill depth h_s increases and internal wave propagation over the sill can occur, leading to a reduction of wave overturning and breaking and associated upper water column mixing found in the earlier calculations.

5. CONCLUDING REMARKS

Earlier work (XD06, DX07) that was concerned with the role of small scale topography, such as localized ripples that are found on sills, or changes in vertical stratification in sill regions, is extended here to examine the role of bottom turbulent mixing of tidal origin, and water depth in the region of sills. In particular the influence of enhanced bed friction and associated turbulence due to changes in bed roughness reflecting differences in bed types (e.g. sand or gravel) often found in sill regions is considered. As bed roughness increases going from a sand to gravel regime so does bed turbulence, parameterized here in terms of vertical eddy viscosity. The effects of both changes in bed friction and vertical eddy viscosity together with water depth upon mixing and internal wave generation were examined in shallow sill regions. Transfer of energy from the barotropic M_2 tide into a spectrum of internal waves was quantified in terms of energy power spectra, with spatial distributions of R_i number and isotherms quantifying the degree of mixing.

In order to determine the influence of bottom friction coefficient, eddy viscosity and water depth, idealized sill topography representing a symmetric sill was used, rather than the Loch Etive topography considered in XD06, DX07. However the main features of the topography were such as to represent a sill in a Loch, or a small bank in a shallow sea region.

All calculations were performed using a cross sectional non-hydrostatic model, with sinusoidal forcing at the M_2 period. The buoyancy frequency was fixed as was the sill topography, except when the water depth was changed, when the aspect ratio of the top of the sill was maintained. By this means changes in friction coefficient, eddy viscosity and water depth could be assessed, while maintaining the same sill Froude number F_s.

In an initial calculation water depth was 100 m, bottom friction k = 0.0025, with A_v = 0.001 $m^2 s^{-1}$ typical values in sill regions (XD06). Calculations showed a hydraulic transition in the upper part of the water column, with lee waves and a current jet produced near the top of the sill which was 85 m above the bed. Away from the sill region there was no significant flow in the bottom half of the water column and hence bottom frictional effects had no influence. However over the sill top, currents were significant and bottom friction together with vertical eddy viscosity determined vertical shear in the current profile. The shallow nature of the sill (h_s = 15 m) prevented internal waves propagating over the sill, and significant internal mixing occurred on the downstream side of the sill at a depth below the surface approximately equal to the sill depth. This mixing was clearly evident in the distribution of isotherms and R_i numbers downstream of the sill. Although there was limited bottom boundary layer mixing on top of the sill this was absent downstream of the sill. Internal wave spectra downstream of the sill showed a strong lee wave signal and the presence of an internal tide.

Increasing the bottom friction coefficient to k = 0.025, modified the current profile over the sill due to bottom frictional effects. This gave rise to a stronger lee wave signal and increased internal mixing on the lee side of the sill, although away from the sill the flow at depth and hence bottom mixing was zero. Power spectra showed a slight reduction in internal tide generation with more energy in the high frequency lee wave part of the spectrum and enhanced mixing.

Calculations showed that maintaining k at 0.0025, but increasing A_v only slightly modified the across sill flow profile, namely a small reduction in bed shear. However there was a significant reduction in the lee wave signal and hence internal mixing on the lee side of the sill. As previously away from the sill, currents in the lower half of the water column and hence bottom frictional effects and bottom mixing were zero. Downstream of the sill, internal mixing was confined to the sill region and was weak.

Power spectra showed that as A_v increased the energy in the lee wave band decreased. Initially this decrease was greatest at frequencies removed from the dominant lee wave frequency leading to a sharpening in the spectrum at this frequency. However, as vertical viscosity increased, energy in the lee wave band rapidly decreased.

These calculations in which the sill top was well removed from the sea bed, namely sill height $h_o \approx h$, clearly show that bottom boundary layer effects and mixing downstream of the sill were zero. However bottom frictional effects and associated turbulence on the top of the sill were important, with vertical eddy viscosity influencing lee wave generation and associated internal mixing.

In subsequent calculations the water depth was reduced to h = 50 m while maintaining the sill depth at h_s = 15 m and hence h_o = 35 m. In this case the top of the sill was close to the seabed. Calculations with k = 0.0025 and A_v = 0.001 m^2 s^{-1}, with U_o adjusted to give the same across sill velocity and hence sill Froude number F_s, as in the deep water case, showed that although the profile and magnitude of the across sill velocity were in good agreement with those used in the deep water case, lee wave generation was significantly reduced due to the decrease in water depth. In addition the region of non-zero velocity now extended throughout the water column, and there was significant bottom mixing in the lee of the sill, which extended throughout the water column, as shown in the R_i number distributions. Power spectra did not show a peak at the lee wave frequency but a gradual decrease of energy with frequency suggesting significant mixing. As in the deep water calculations, increasing A_v reduced shear in the bottom boundary layer on top of the sill, and reduced lee wave generation.

These calculations clearly show that for the same across sill flow, and sill aspect ratio, lee wave production on the lee side of the sill is reduced as water depth is decreased. In addition when the sill height h_o is small there is significant bottom mixing downstream of the sill. In the case in which the water depth is comparable to h_o, mixing in the downstream sill region extends throughout the water column. However calculations in which h_o was comparable to the height of the bottom boundary layer, but the water was deep, suggested that mixing was confined to the bottom boundary layer with the water above this remaining stratified. In this case, namely $h_o < h$ and $h_s \approx h$, internal waves could propagate over the sill, and internal wave spectra from the sill top showed an appreciable internal tide signal in this region with some lee wave propagation over the sill. In this case the lee wave propagated over the sill rather than producing internal mixing that was near zero, while bottom mixing downstream of the sill was the main mixing agent. The degree to which h_s influences across sill propagation of lee waves and hence internal mixing is beyond the scope of the present paper but is being examined.

Calculations presented here clearly show that when h_o is comparable to h, and exceeds the thickness of the turbulent bottom boundary layer, then for given N, values of k and A_v (which are related to bed roughness) on top of the sill will control internal mixing downstream of the sill. In very shallow water the bed roughness and associated turbulence both on the sill and downstream of the sill are important in determining lee wave production and sill mixing. Consequently bed roughness and the associated turbulence in sill regions together with velocity, stratification and detailed topography need to be measured in order to provide data sets for rigorous model validation. In the case in which h_s is sufficiently large to permit internal wave propagation across the sill to occur, then internal wave measurements both on top of the sill besides on its leeward side are required.

ACKNOWLEDGEMENTS

The authors are indebted to L. Parry and E. Ashton for typing the text and R. A. Smith for help in figure preparation.

REFERENCES

Adcroft, A., C. Hill and J. Marshall (1997) Representation of topography by shaved cells in a height coordinate ocean model. Monthly Weather Review, 125, 2293-2315.

Baines, P.G. (1995) Topographic effects on stratified flows. Cambridge Monographs on Mechanics. Cambridge University Press.

Berntsen, J., J. Xing and G. Alendal (2006) Assessment of non-hydrostatic ocean models using laboratory scale problems. Continental Shelf Research, 26, 1433-1447.

Davies, A.M. and J.E. Jones (1990) Application of a three-dimensional turbulence energy model to the determination of tidal currents on the northwest European shelf. Journal of Geophysical Research, 95, 18143-18162.

Davies, A.M. and J. Xing (2004) Modelling processes influencing wind induced internal wave generation and propagation. Continental Shelf Research, 24, 2245-2271.

Davies, A.M. and J. Xing (2005) The effect of a bottom shelf front upon the generation and propagation of near-inertial internal waves in the coastal ocean. Journal of Physical Oceanography (35), 6, 976-990.

Davies, A.M. and J. Xing (2007) On the influence of stratification and tidal forcing upon mixing in sill regions. Ocean Dynamics. Ocean Dynamics, 57, 431-451.

Dewey, R. D. Richmond and C. Garrett (2005) Stratified tidal flow over a bump. Journal of Physical Oceanography, 35, 1911-1927.

Gerkema, T. and J.T.F. Zimmerman (1995) Generation of non-linear internal tides and solitary waves. Journal of Physical Oceanography, 25, 1081-1094.

Gerkema, T. (2001) Internal and interfacial tides: beam scattering and local generation of solitary waves. Journal of Marine Research, 59, 227-251.

Gerkema, T. (2002) Application of an internal tide generation model to baroclinic spring-neap cycles. Journal of Geophysical Research, 107(C9), 3124, doi:10.1029/2001JC001177.

Gillibrand, P.A. and T.L. Amundrud (2007) A numerical study of the tidal circulation and buoyancy effects in a Scottish fjord: Loch Torridon. Journal of Geophysical Research, 112, C05030, doi:10.1029/2006JC003806.

Hosegood, P. and Var Haren, H. (2004) Near bed solibores over the continental slope in the Faeroe-Shetland Channel. Deep Sea Research, 51, 2943-2971.

Inall, M.E., F.R. Cottier, C. Griffiths and T.P. Rippeth (2004) Sill dynamics and energy transformation in a jet fjord. Ocean Dynamics, 54, 307-314.

Inall, M.E., T.P. Rippeth, C. Griffiths and P. Wiles (2005) Evolution and distribution of TKE production and dissipation within stratified flow over topography. Geophys. Res. Lett., 32, L08607, doi:10.1029/2004GL022289.

Jeans, D.R.G. and T.J. Sherwin (2001a) The evolution and energetics of large amplitude non-linear internal waves on the Portuguese shelf. Journal of Marine Research, 59, 327-353.

Jeans, D.R.G. and T.J. Sherwin (2001b) The variability of strongly non-linear solitary internal waves observed during an upwelling season on the Portuguese shelf. Continental Shelf Research, 21, 1855-1878.

Legg, S. and A. Adcroft (2003) Internal wave breaking at concave and convex continental slopes. Journal of Physical Oceanography, 33, 2224-2246.

Legg, S. (2004a) Internal tides generated on a corrugated slope. Part I: Cross-slope barotropic forcing. Journal of Physical Oceanography, 34, 156-173.

Legg, S. (2004b) Internal tides generated on a corrugated continental slope. Part II. Along-slope barotropic forcing. Journal of Physical Oceanography, 34, 1824-1838.

Marshall, J., C. Hill, L. Perelman and A. Adcroft (1997a) Hydrostatic, quasi-hydrostatic and nonhydrostatic ocean modelling. J. Geophys. Res., 102, 5733-5752.

Marshall, J., A. Adcroft, C. Hill, L. Perelman and C. Heisey (1997b) A finite-volume incompressible Navier Stokes model for studies of the ocean on parallel computers. Journal Geophhysical Research, 102, 5753-5766.

Moum, J.N. and Nash, J.D.(2000) Topographically induced drag and mixing at a small bank on the continental shelf. Journal of Physical Oceanography, 30, 2049-2054.

New, A.L. and R.D. Pingree (1990) Evidence for internal tidal mixing near the shelf break in the Bay of Biscay. Deep-Sea Research, 37, 1783-1803.

Rippeth, T.P., M.R. Palmer, J.H. Simpson, N.R. Fisher and J. Sharples (2005) Thermocline mixing in summer stratified continental shelf seas. Geophyscal Research Letters, 32 L05602, doi:10.1029/2004GL022104.

Saenko, O.A. and Merrifield, W.J. (2005) On the effect of topographically enhanced mixing on the global ocean circulation. Journal of Physical Oceanography, 35, 826-834.

Saenko, O.A. (2006) The effect of localized mixing on the Ocean Circulation and time-dependent climate change. Journal of Physical Oceanography, 36, 140-160.

Samelson, R.M. (1998) Large scale circulation with locally enhanced vertical mixing. Journal of Physical Oceanography, 28, 712-726.

Spall, M.A. (2001) Large scale circulations forced by localized mixing over a sloping bottom. Journal of Physical Oceanography, 31, 2369-2384.

Stigebrandt, A. (1999) Resistance to barotropic tidal flow in straits by baroclinic wave drag. Journal of Physical Oceanography, 29, 191-197.

Van Haren, H. and J. Howarth (2004) Enhanced stability during reduction of stratification in the North Sea. Continental Shelf Research, 24, 805-819.

Van Haren, H. (2004) Spatial variability of deep-ocean motions above an abyssal plain. Journal of Geophysical Research, 109, C12014, doi:10.1029/2004JC002558.

Vlasenko, V., Stashchuk, N. and Hutter, K (2005) Baroclinic tides: Theoretical modelling and observational evidence. Cambridge University Press.

Vlasenko, V. and N. Stashchuk (2006) Amplification and suppression of internal waves by tides over variable bottom topography. Journal of Physical Oceanography, 36, 1959-1973.

Xing, J. and A.M. Davies (2001) A three-dimensional baroclinic model of the Irish Sea: formation of the thermal fronts and associated circulation. Journal of Physical Oceanography, 31, 94-114.

Xing, J. and A.M. Davies (2005) Influence of a cold water bottom dome on internal wave trapping. Geophysical Research Letters, 32, L03601, doi:10.1029/2004GL021833.

Xing, J. and A.M. Davies (2006a) Internal wave trapping and mixing in a cold water dome, Journal of Geophysical Research, 111, C07002, doi:10.1029/2005JC003417.

Xing, J. and A.M. Davies (2006b) Processes influencing tidal mixing in the region of sills. Geophysical Research Letters, (33), L04603, doi:10.1029/2005GL025226.

Xing, J. and Davies, A.M. (2006c) Influence of stratification and topography upon internal wave spectra in the region of sills. Geophysical Research Letters, 33, L23606, doi:10.1029/ 2006GL028092.

Xing, J. and A.M. Davies (2007) On the importance of non-hydrostatic processes in determining tidal induced mixing in sill regions, Continental Shelf Research, 27, 2162-2185.

Zhai, X., R.J. Greatbatch and J. Zhao (2005) Enhanced vertical propagation of storm-induced near-inertial energy in an eddying ocean channel model. Geophysical Research Letters, 32, L18602, doi: 10.1029/2005GL023643.

FIGURE CAPTIONS

Fig. 1: Initial temperature distribution (°C) (contour interval, c.i. = 0.25) in the sill region, with centre of sill at x = 0, for (a) water depth of 100 m, and (b) water depth of 50 m.

Fig. 2a: Sub-domain of the region showing temperature field (°C, c.i. = 0.25), u velocity (cm s^{-1}, c.i. = 5) and w vertical velocity (cm s^{-1}, c.i. = 2) at t = 8/8T (where T is tidal period), from Calc 1 (Table 1).

Fig. 2b: As Fig. 2a, but at t = 16/8T.

Fig. 2c: Contours of R_i number (shaded) and temperature (°C, c.i. = 0.5) over a sub-domain of the region at t = 8/8T, from Calc. 1.

Fig. 2d: As Fig. 2c but at t = 16/8T.

Fig. 3a: Time series of temperature (°C, c.i. = 0.5), u velocity (cm s^{-1}, c.i. = 5) over the first two tidal cycles at x = 0, from Calc. 1.

Fig. 3b: As Fig. 3a and for vertical velocity w (cm s^{-1}, c.i. = 2) at x = 500 m.

Fig. 4: Depth integrated power spectra of vertical velocity w at frequencies normalized with respect to the M_2 tide computed at x = 500 m for (a) h = 100m, k = 0.0025, A_v = 0.001 m^2 s^{-1} (Calc 1), (b) h = 100m, k = 0.025, A_v = 0.001 m^2 s^{-1} (Calc 2), (c) h = 100m, k = 0.025, A_v = 0.005 m^2 s^{-1} (Calc 3), (d) h = 100m, k = 0.0025, A_v = 0.01 m^2 s^{-1} (Calc 4), (e) h = 50m, k = 0.0025, A_v = 0.001 m^2 s^{-1} (Calc 5,) (f) h = 50m, k = 0.0025, A_v = 0.01 m^2 s^{-1} (Calc 6).

Fig. 5a: Sub-domain of the region showing the temperature field (°C, c.i. = 0.25), u velocity (cm s^{-1}, c.i. = 5) and w velocity (cm s^{-1}, c.i. =2) at t = 8/8T, from Calc. 2.

Fig. 5b: As Fig. 5a, but at t = 16/8T.

Fig. 5c: Contours of R_i number (shaded) and temperature (°C, c.i. = 0.5) over a sub-domain of the region at t = 8/8T, from Calc. 2.

Fig. 6a: Sub-domain of the region showing temperature field (°C, c.i. = 0.25), u velocity (cm s^{-1}, c.i. = 5) and w velocity (cm s^{-1}, c.i. = 2) at t = 8/8T from Calc. 3.

Fig. 6b: Contours of R_i number (shaded) and temperature (°C, c.i. = 0.5) over a sub-domain of the region at t = 8/8T from Calc. 3.

Fig. 6c: Time series of temperature (°C, c.i. = 0.5), u velocity (cm s^{-1}, c.i. = 5) over the first two tidal cycles at x = 0, from Calc. 3.

Fig. 6d: As Fig. 6c but at x = 500 m.

Fig. 7a: Sub-domain of the region showing temperature field (°C, c.i. = 0.25), u velocity (cm s^{-1}, c.i. = 5) at t = 8/8T from Calc. 4.

Fig. 7b: Time series of temperature (°C, c.i. = 0.5), u velocity (cm s^{-1}, c.i. = 5) over the first two tidal cycles at x = 0, from Calc . 4.

Fig. 8a: Sub-domain of the region showing temperature field (°C, c.i. = 0.25), u velocity (cm s^{-1}, c.i. = 5) at t = 8/8T from Calc. 5.

Fig. 8b: As Fig. 8a, but at t = 16/8T.

Fig. 8c: Contours of R_i number (shaded) and temperature (°C, c.i. = 0.5) over a sub-domain of the region at t = 8/8T from Calc. 5.

Fig. 8d: As Fig. 8c, but at t = 16/8T.

Fig. 9a: Time series of temperature (°C, c.i. = 0.5), u velocity (cm s^{-1}, c.i. = 5) over the first two tidal cycles at x = 0 from Calc. 5.

Fig. 9b: As Fig. 9a, but at x = 500 m.

Fig. 10a: Sub-domain of the region showing temperature field (°C, c.i. = 0.25), u velocity (cm s^{-1}, c.i. = 5) and w velocity (cm s^{-1}, c.i. = 2) at t =16/8T from Calc 6.

Fig. 10b: Contours of R_i number (shaded) and temperature (°C, c.i. = 0.5) over a sub-domain of the region at t = 16/8T from Calc. 6.

Fig. 10c: Time series of temperature (°C, c.i. = 0.5) over the first two tidal cycles at x = 0, from Calc. 6.

Fig. 11a: Sub-domain of the region showing temperature field (°C, c.i. = 0.5), u velocity (cm s^{-1}, c.i. = 5) and w velocity (cm s^{-1}, c.i. = 2) at t = 8/8T from Calc. 7.

Fig. 11b: Contours of R_i number (shaded) and temperature (°C, c.i. = 0.5) over a sub-domain of the region at t = 8/8T from Calc. 7.

Fig. 12: Time Series of temperature (°C, c.i. = 0.5), u velocity (cm s^{-1}, c.i. = 2) over the first two tidal cycles at x = 0 from Calc. 7.

Fig. 13: Depth integrated power spectra of vertical velocity w at frequencies normalized with respect to the M_2 tide computed at (a) x = 0, and (b) x = 500 m from Calc. 7.

TABLE 1: Summary of parameters used in the calculations

Calc	Sill Half Width a_s(m)	Friction Coefficient k	Eddy Viscosity A_v (m^2 s^{-1})	Water Depth h (m)	Sill Height h_o (m)	Sill Depth h_s (m)
1	500	0.0025	0.001	100	85	15
2	500	0.025	0.001	100	85	15
3	500	0.0025	0.005	100	85	15
4	500	0.0025	0.01	100	85	15
5	V	0.0025	0.001	50	35	15
6	V	0.0025	0.01	50	35	15
7	V	0.0025	0.001	100	20	80

Note: V denotes variable, see text.

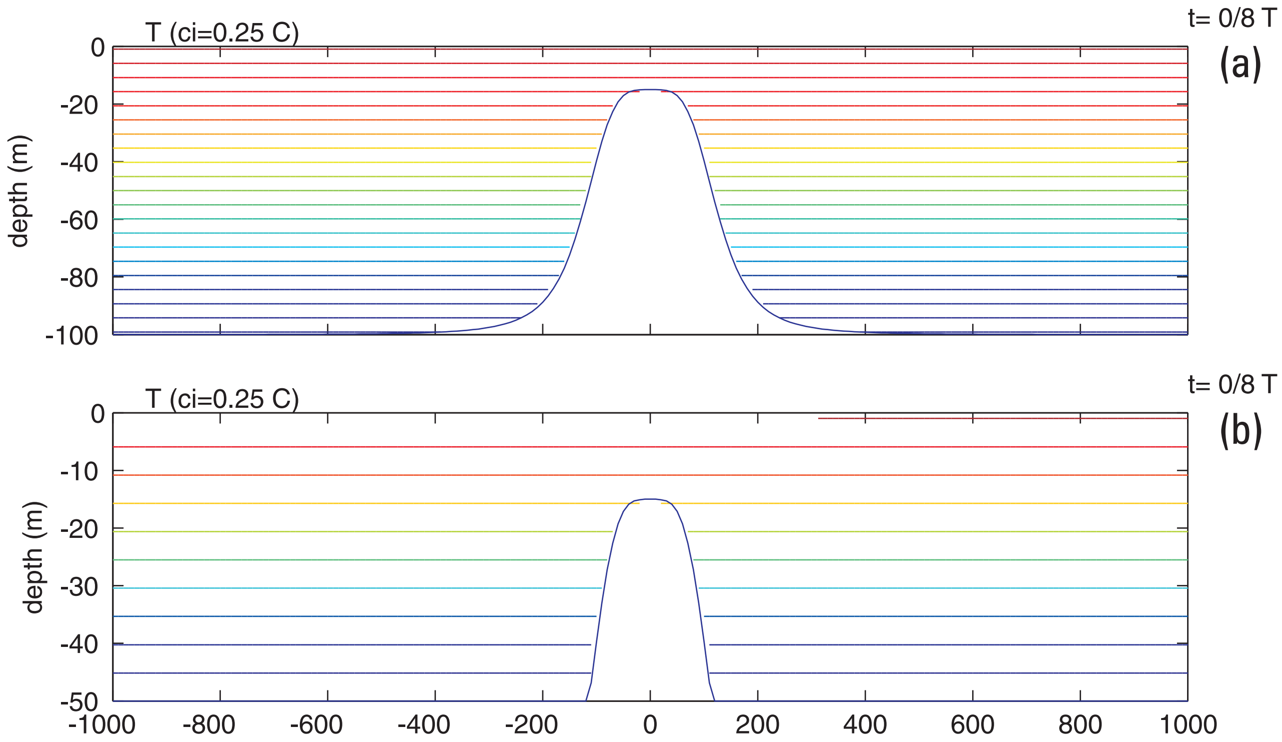
T (ci=0.25 C)
t= 0/8 T
(a)
depth (m)
0
-20
-40
-60
-80
-100
T (ci=0.25 C)
t= 0/8 T
(b)
depth (m)
0
-10
-20
-30
-40
-50
-1000
-800
-600
-400
-200
0
200
400
600
800
1000

Fig 1

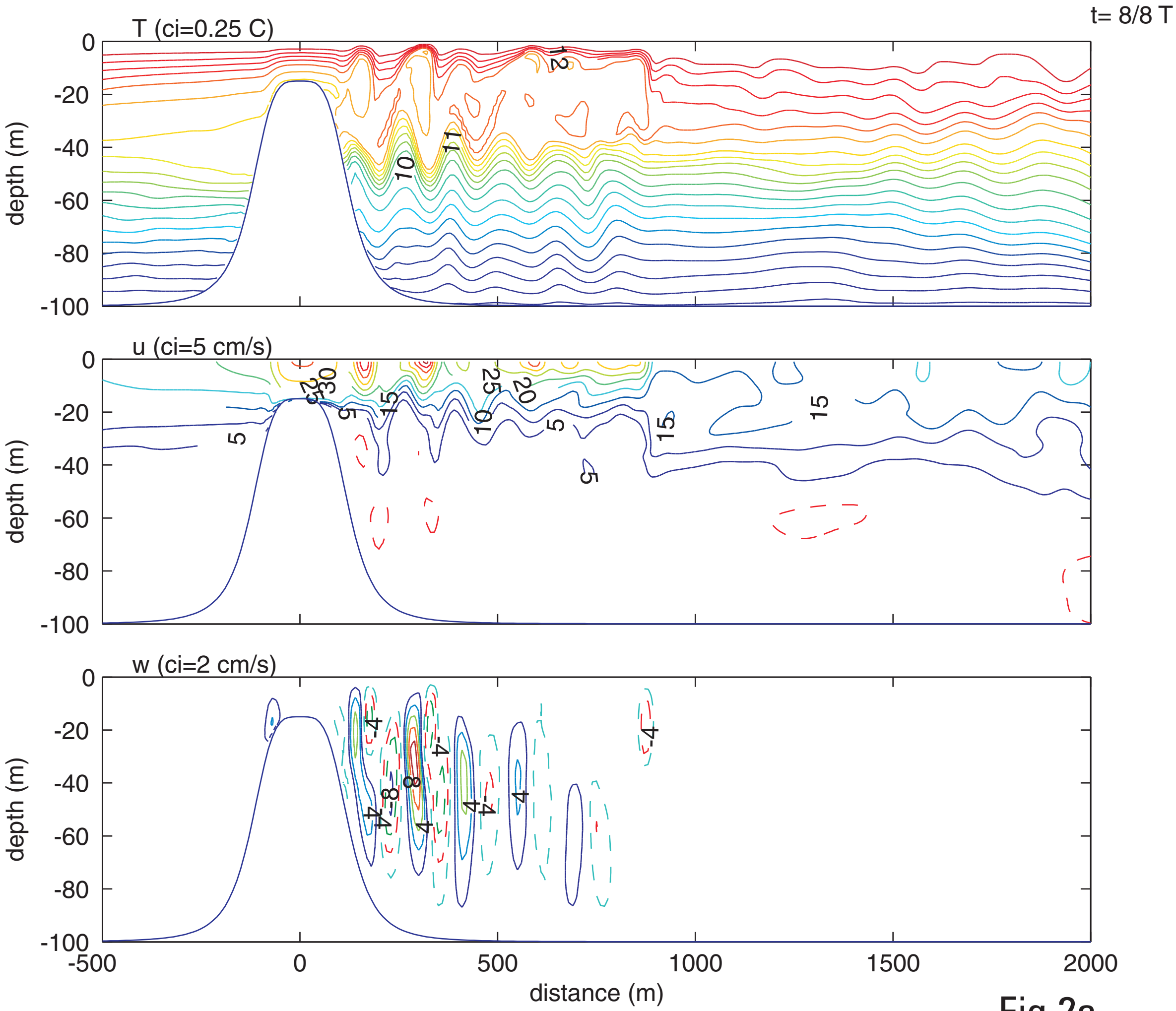
t= 8/8 T
T (ci=0.25 C)
u (ci=5 cm/s)
w (ci=2 cm/s)
depth (m)
distance (m)

Fig 2a

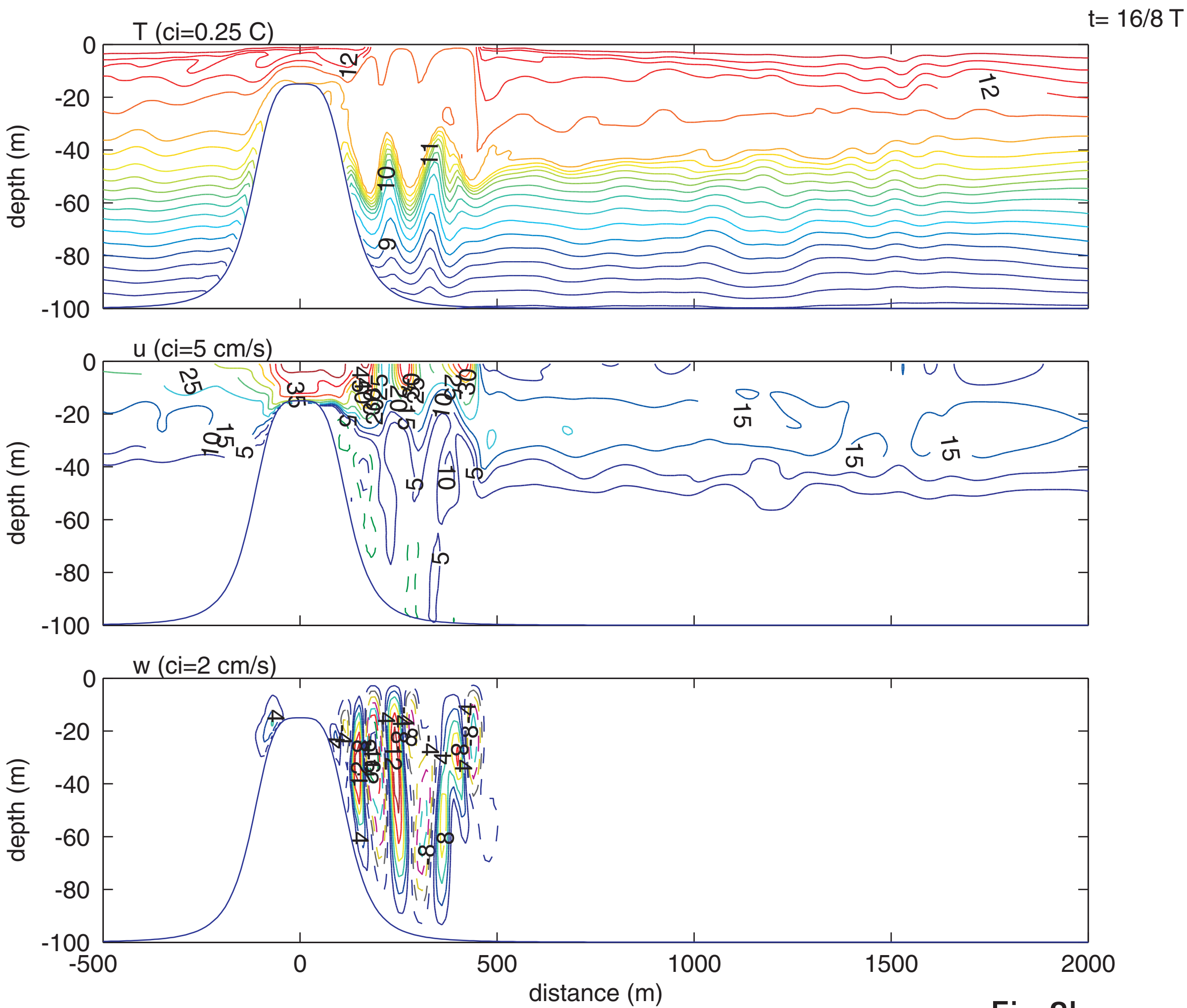
t= 16/8 T
T (ci=0.25 C)
u (ci=5 cm/s)
w (ci=2 cm/s)
depth (m)
distance (m)

Fig 2b

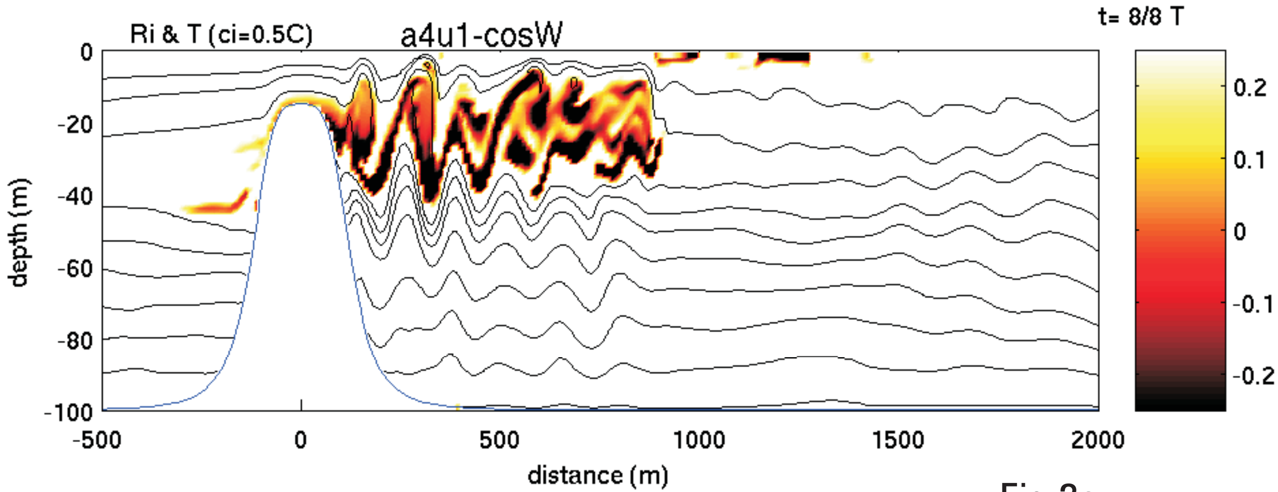

Ri & T (ci=0.5C)
a4u1-cosW
t= 8/8 T
0
-20
-40
-60
-80
-100
depth (m)
-500
0
500
1000
1500
2000
distance (m)
0.2
0.1
0
-0.1
-0.2

Fig 2c

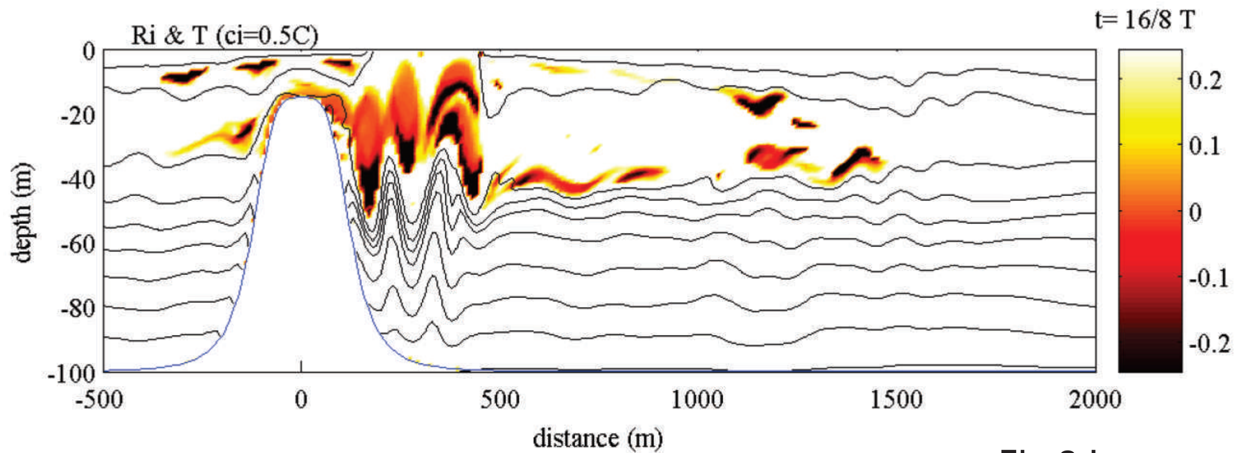

Ri & T (ci=0.5C)
t= 16/8 T
0
-20
-40
-60
-80
-100
depth (m)
-500
0
500
1000
1500
2000
distance (m)
0.2
0.1
0
-0.1
-0.2

Fig 2d

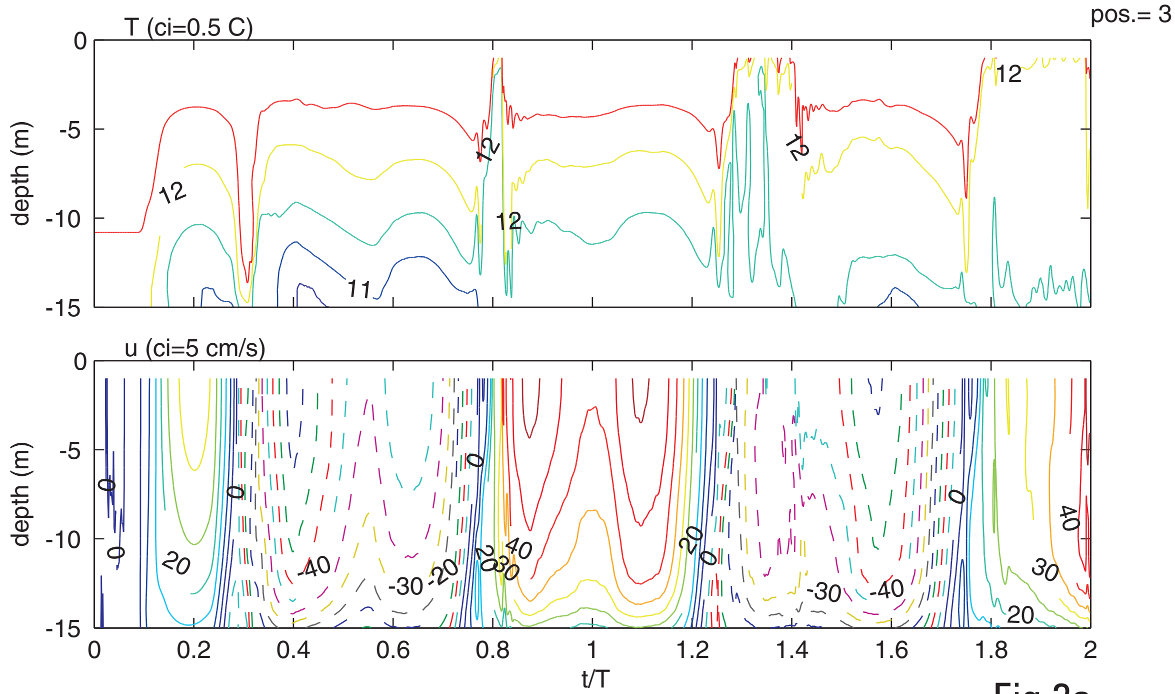
pos.= 3
T (ci=0.5 C)
u (ci=5 cm/s)
depth (m)
t/T

Fig 3a

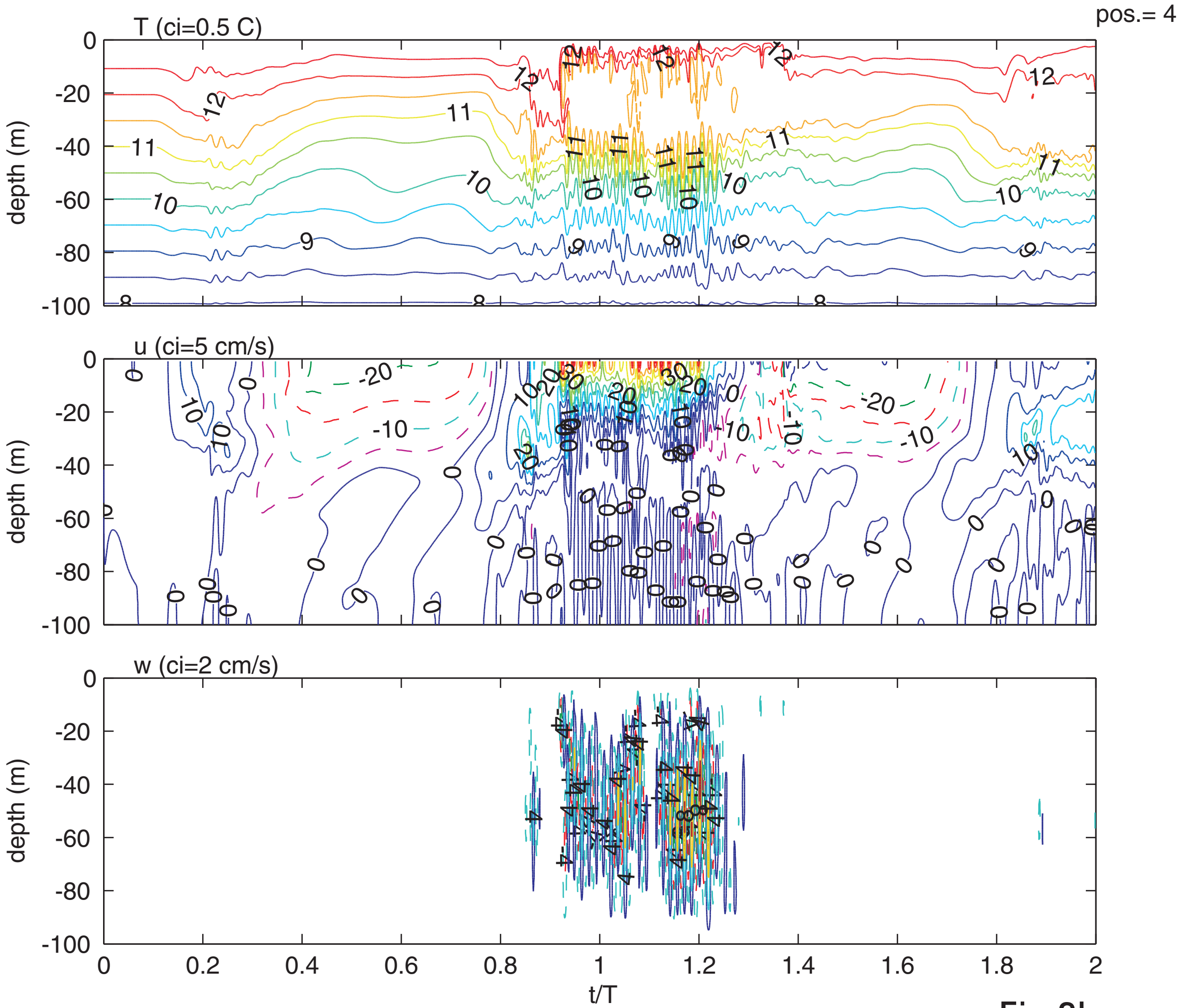
pos.= 4
T (ci=0.5 C)
u (ci=5 cm/s)
w (ci=2 cm/s)
depth (m)
t/T

Fig 3b

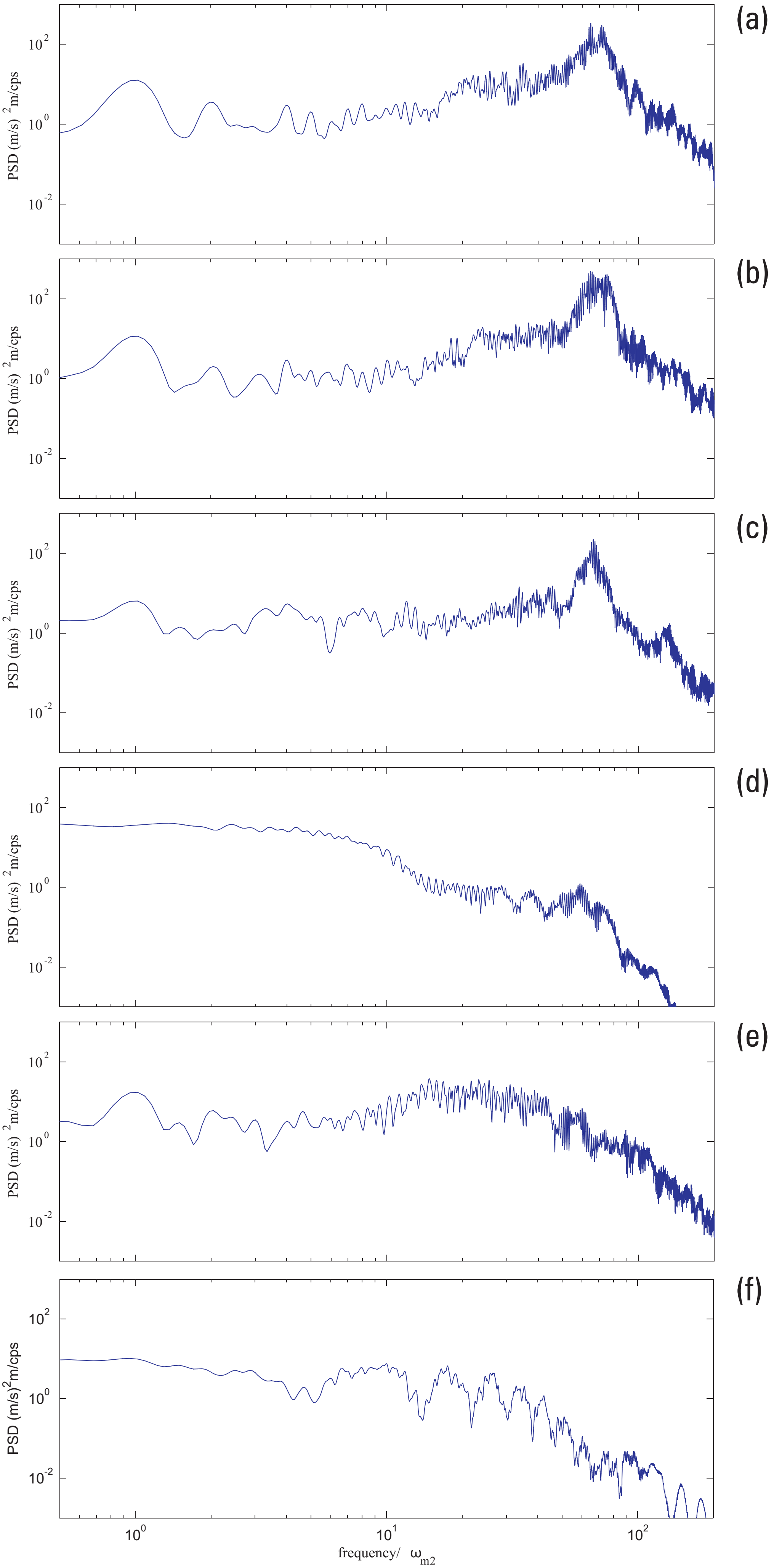

(a)
(b)
(c)
(d)
(e)
(f)
PSD (m/s) ^{2}m/cps
10^2
10^0
10^{-2}
10^0
10^1
10^2
frequency/ ω_{m2}

Fig 4

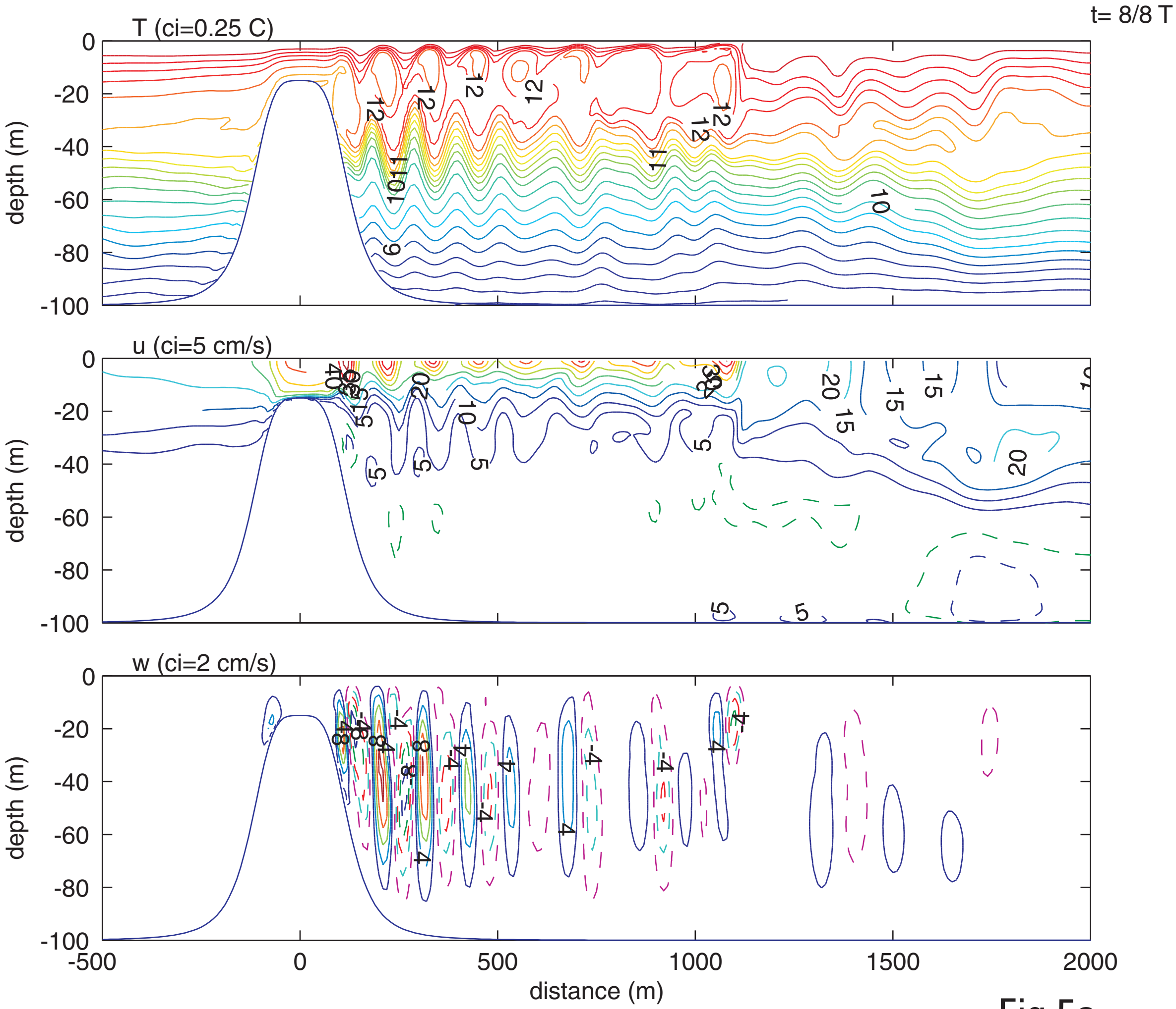
t= 8/8 T
T (ci=0.25 C)
u (ci=5 cm/s)
w (ci=2 cm/s)
depth (m)
distance (m)
Fig 5a

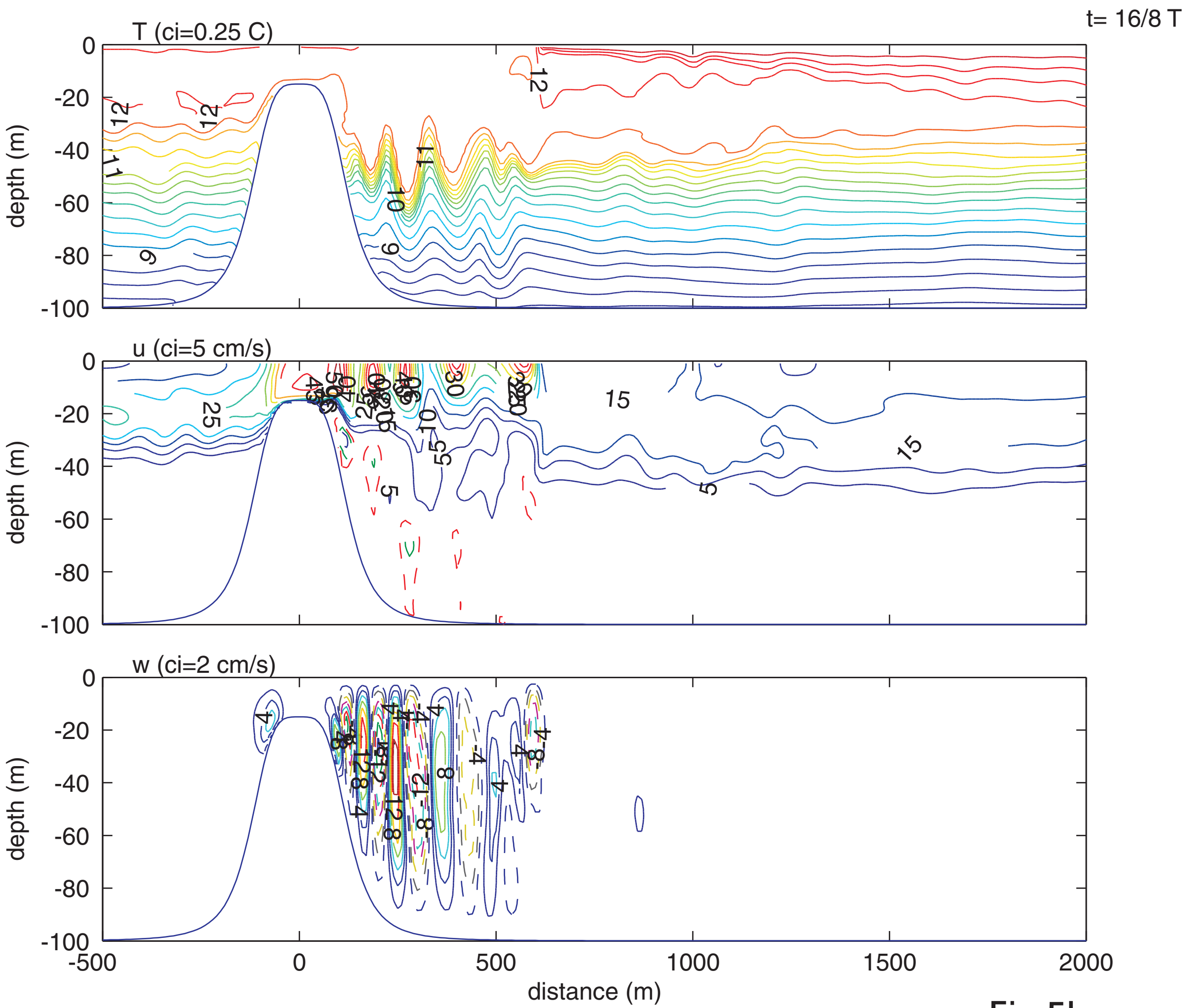
t= 16/8 T
T (ci=0.25 C)
u (ci=5 cm/s)
w (ci=2 cm/s)
depth (m)
distance (m)
Fig 5b

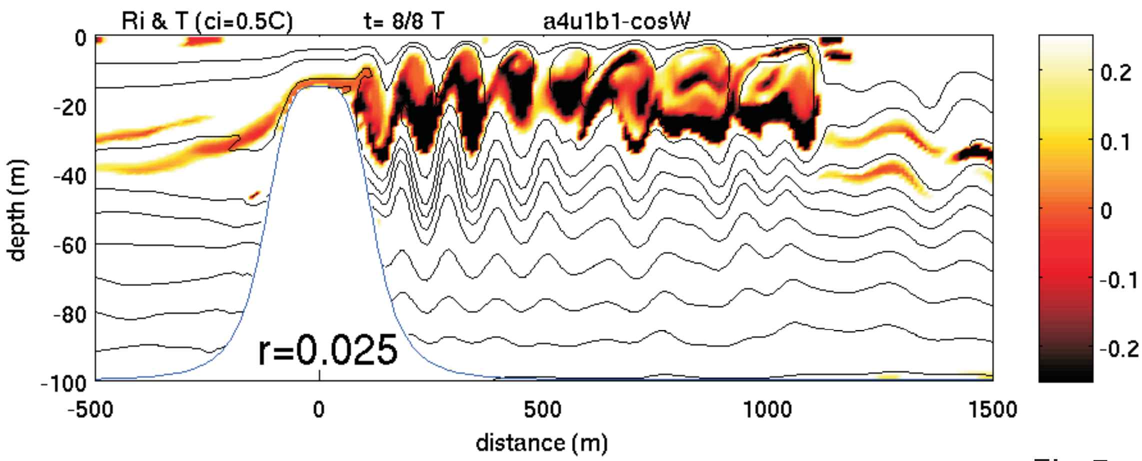

Ri & T (ci=0.5C)
t= 8/8 T
a4u1b1-cosW
depth (m)
distance (m)
r=0.025
0
-20
-40
-60
-80
-100
-500
0
500
1000
1500
0.2
0.1
0
-0.1
-0.2

Fig 5c

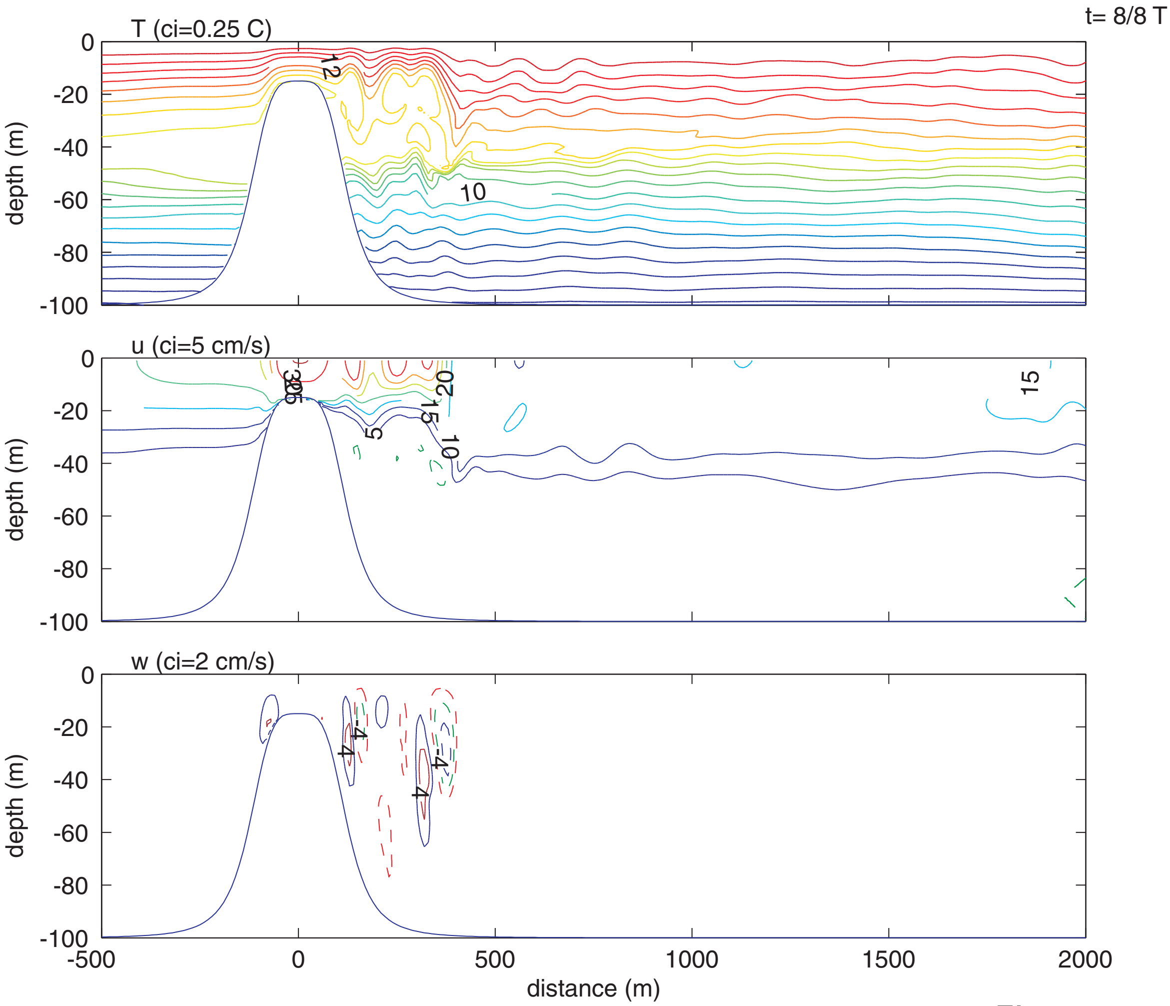

t= 8/8 T
T (ci=0.25 C)
depth (m)
u (ci=5 cm/s)
w (ci=2 cm/s)
distance (m)

Fig 6a

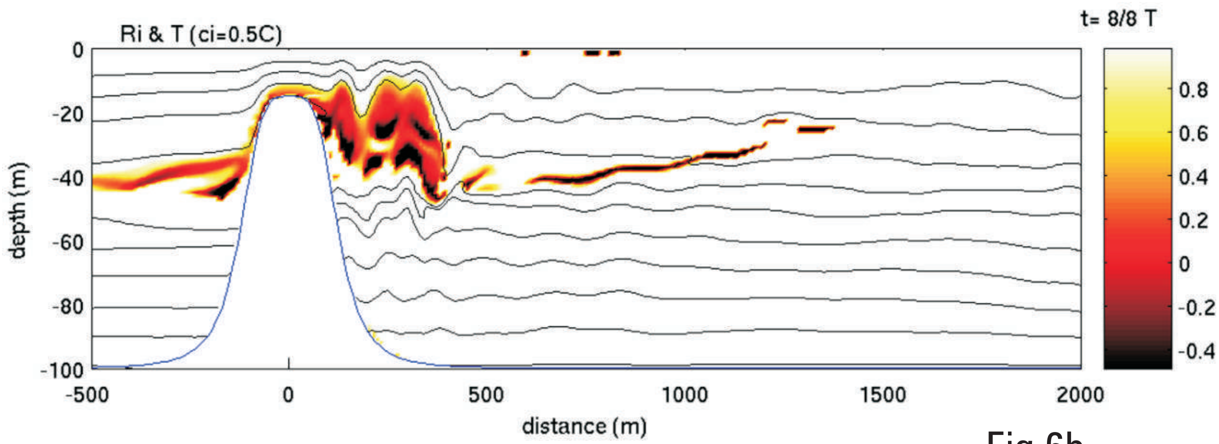

t= 8/8 T
Ri & T (ci=0.5C)
depth (m)
distance (m)

Fig 6b

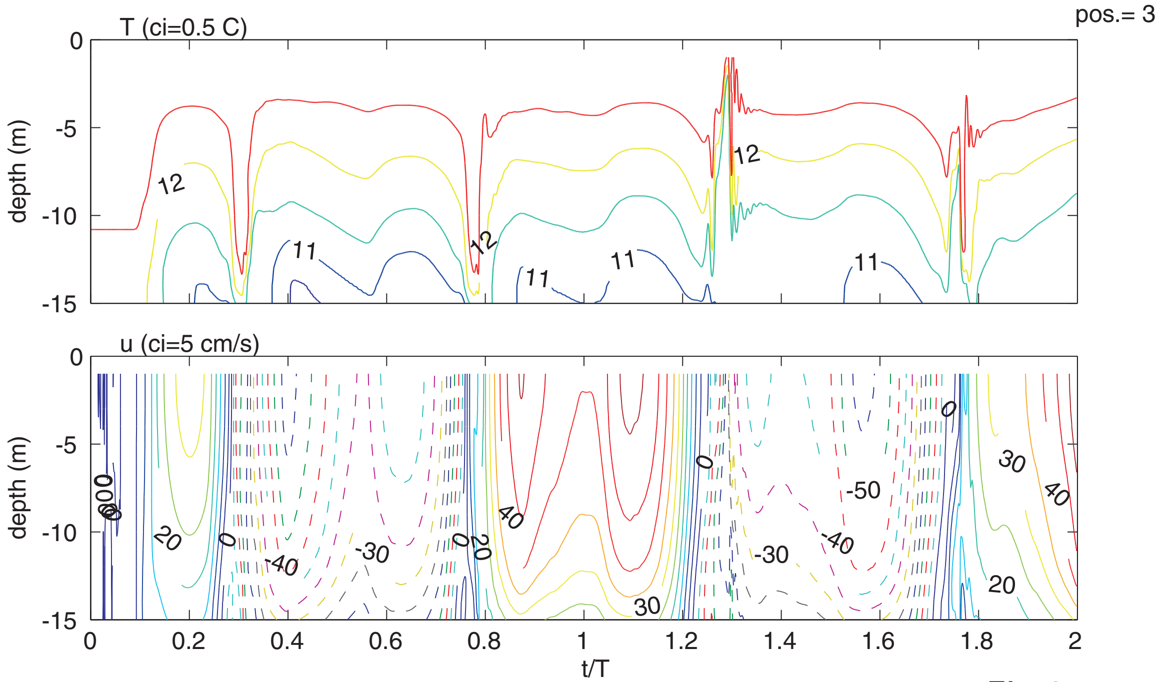
pos.= 3
T (ci=0.5 C)
u (ci=5 cm/s)
depth (m)
t/T

Fig 6c

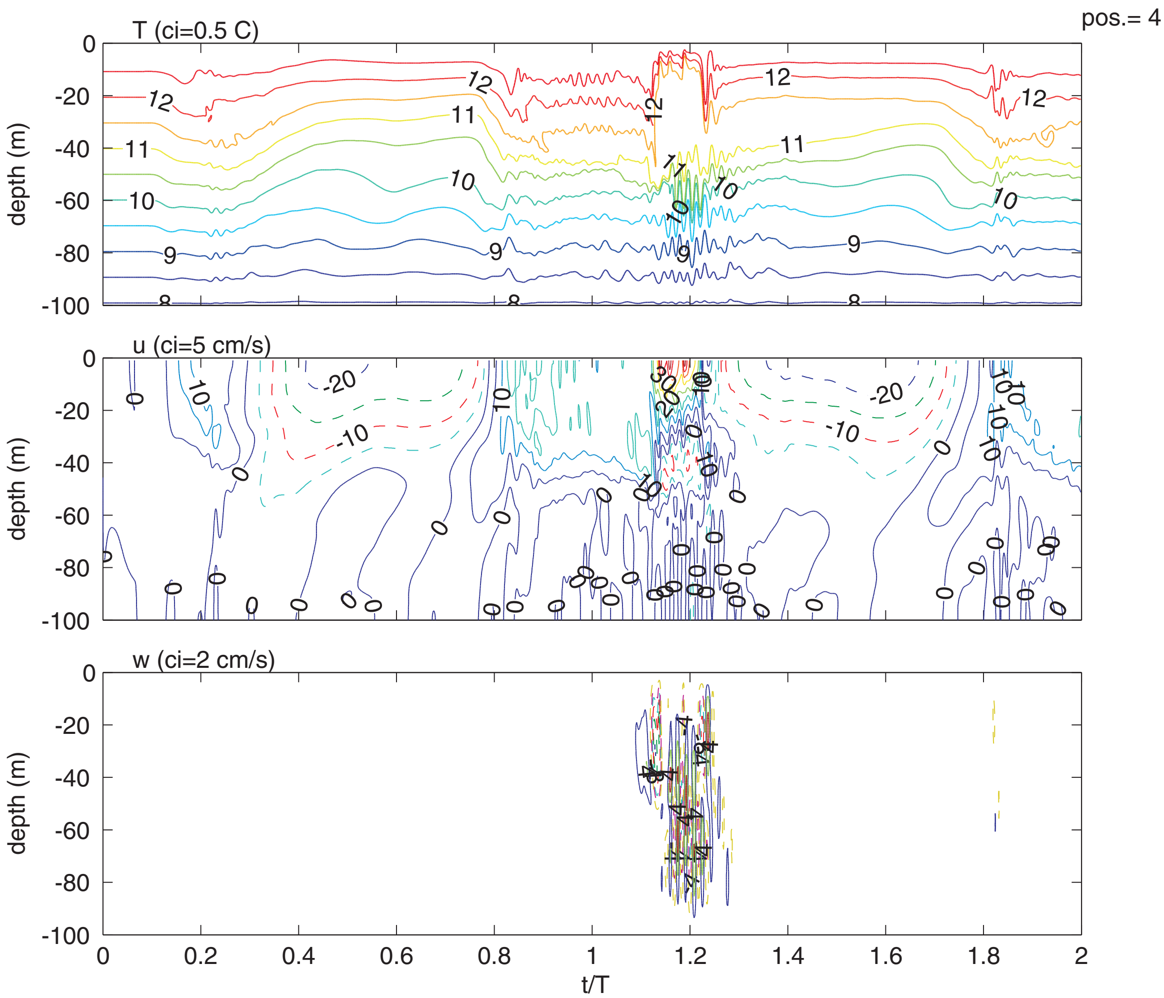
pos.= 4
T (ci=0.5 C)
u (ci=5 cm/s)
w (ci=2 cm/s)
depth (m)
t/T

Fig 6d

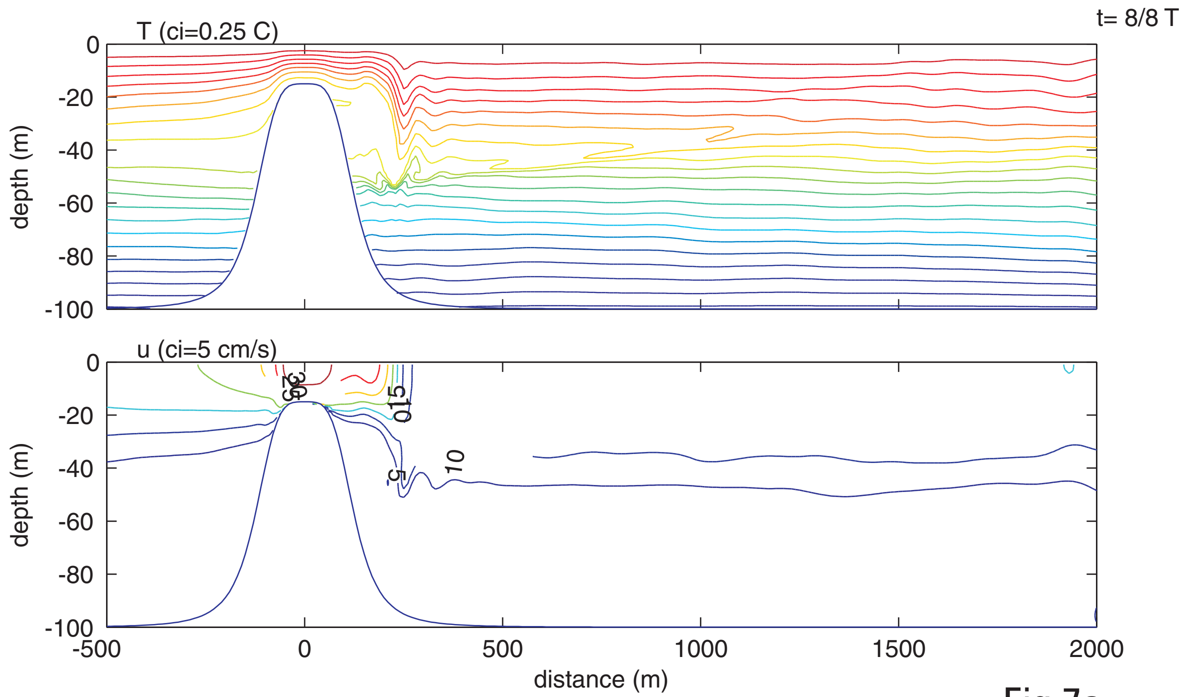
t= 8/8 T
T (ci=0.25 C)
u (ci=5 cm/s)
depth (m)
depth (m)
distance (m)
0
-20
-40
-60
-80
-100
-500
0
500
1000
1500
2000
25
20
15
10
0
5
10

Fig 7a

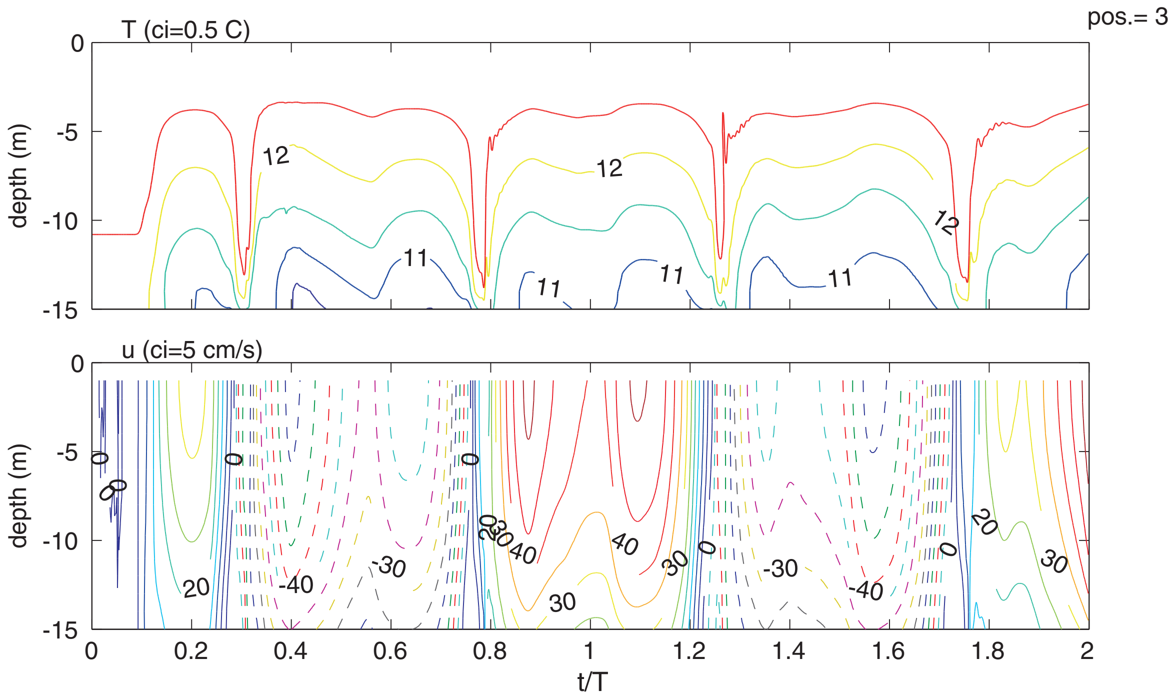
pos.= 3
T (ci=0.5 C)
depth (m)
12
11
u (ci=5 cm/s)
depth (m)
0
20
-40
-30
30
40
t/T
0
-5
-10
-15
0.2
0.4
0.6
0.8
1
1.2
1.4
1.6
1.8
2

Fig 7b

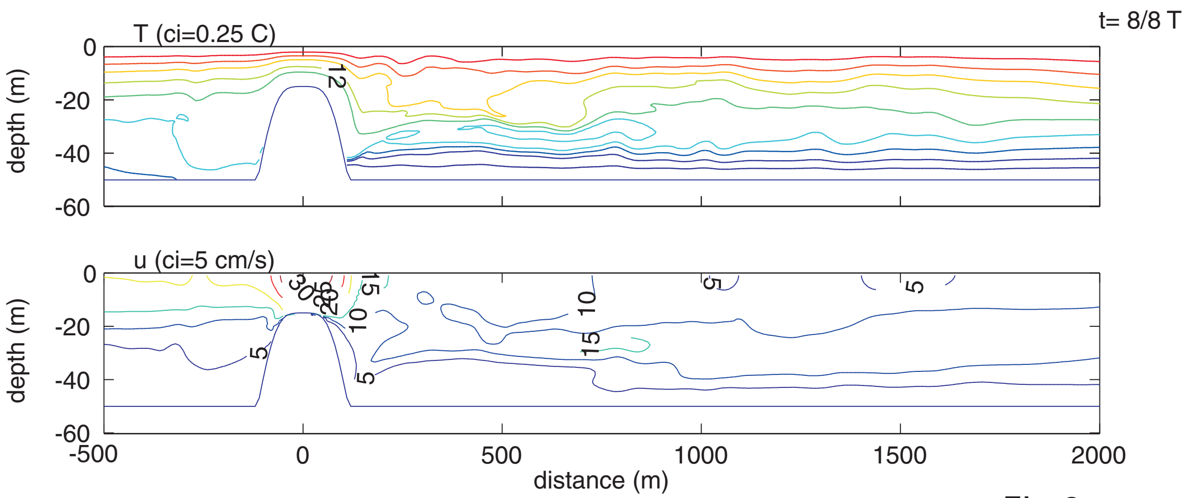

t= 8/8 T
T (ci=0.25 C)
depth (m)
0
-20
-40
-60
12
u (ci=5 cm/s)
30
25
20
15
10
5
-500
0
500
1000
1500
2000
distance (m)

Fig 8a

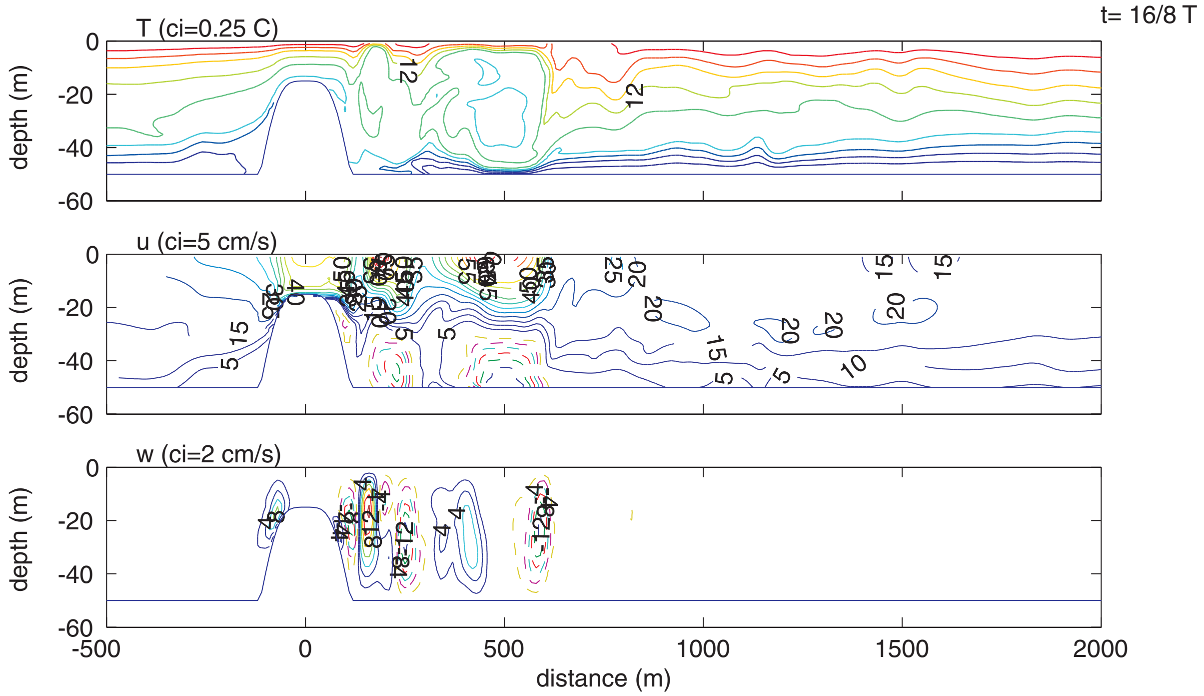

Fig 8b

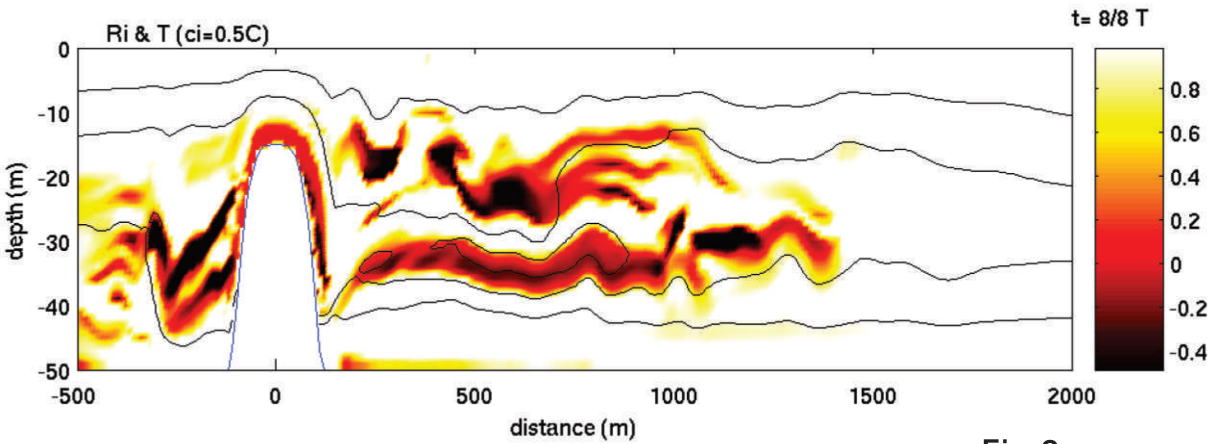
Ri & T (ci=0.5C)
t= 8/8 T
0
-10
-20
-30
-40
-50
depth (m)
-500
0
500
1000
1500
2000
distance (m)
0.8
0.6
0.4
0.2
0
-0.2
-0.4

Fig 8c

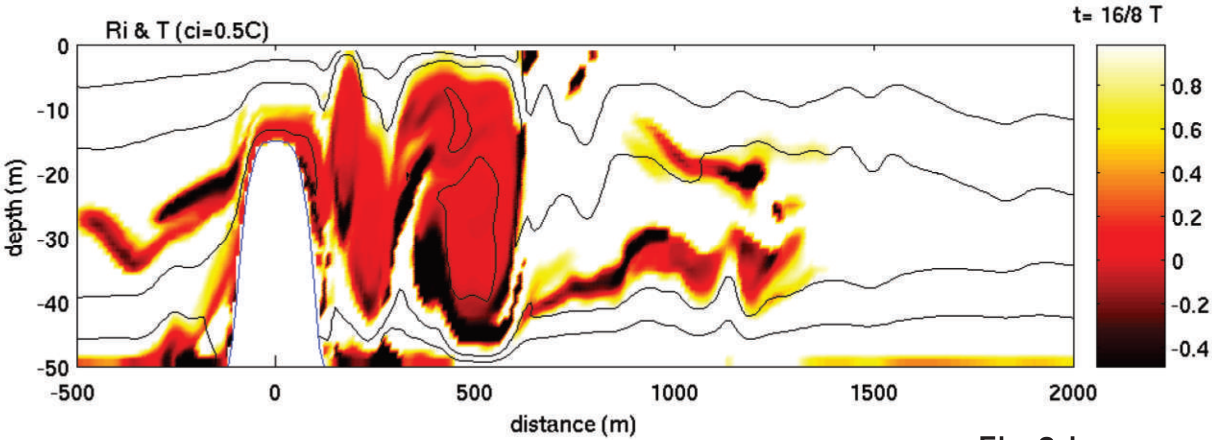
Ri & T (ci=0.5C)
t= 16/8 T
depth (m)
0
-10
-20
-30
-40
-50
-500
0
500
1000
1500
2000
distance (m)
0.8
0.6
0.4
0.2
0
-0.2
-0.4

Fig 8d

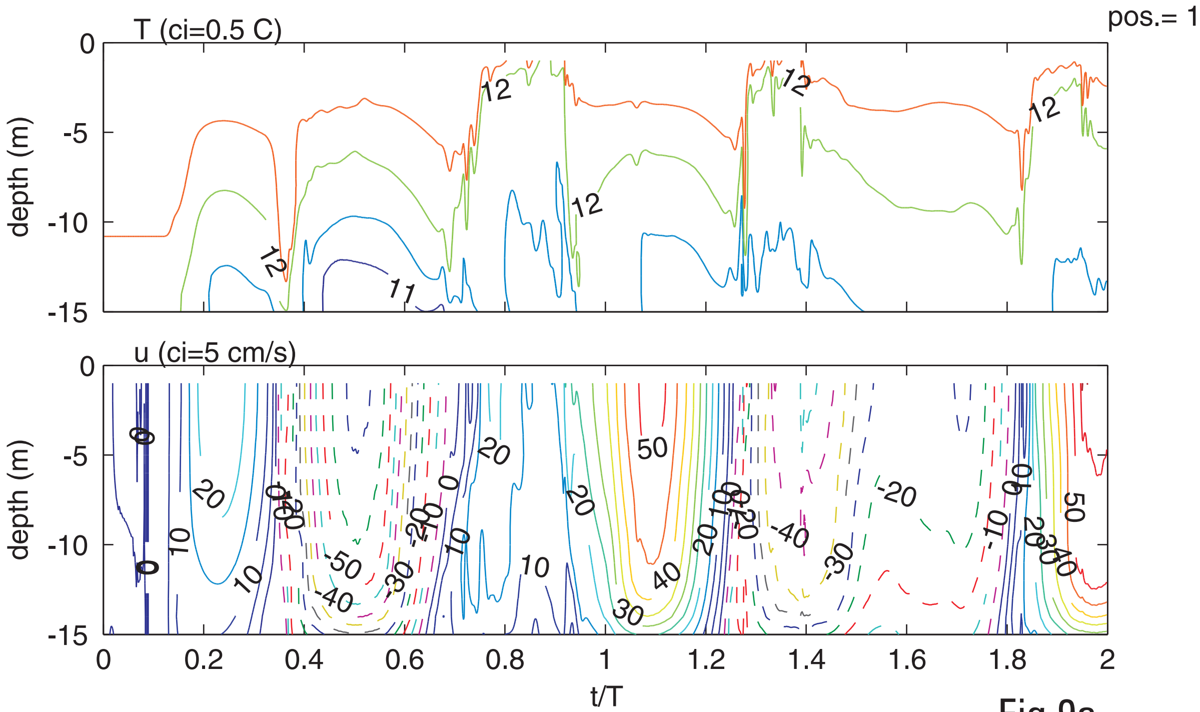
pos.= 1
T (ci=0.5 C)
u (ci=5 cm/s)
depth (m)
t/T

Fig 9a

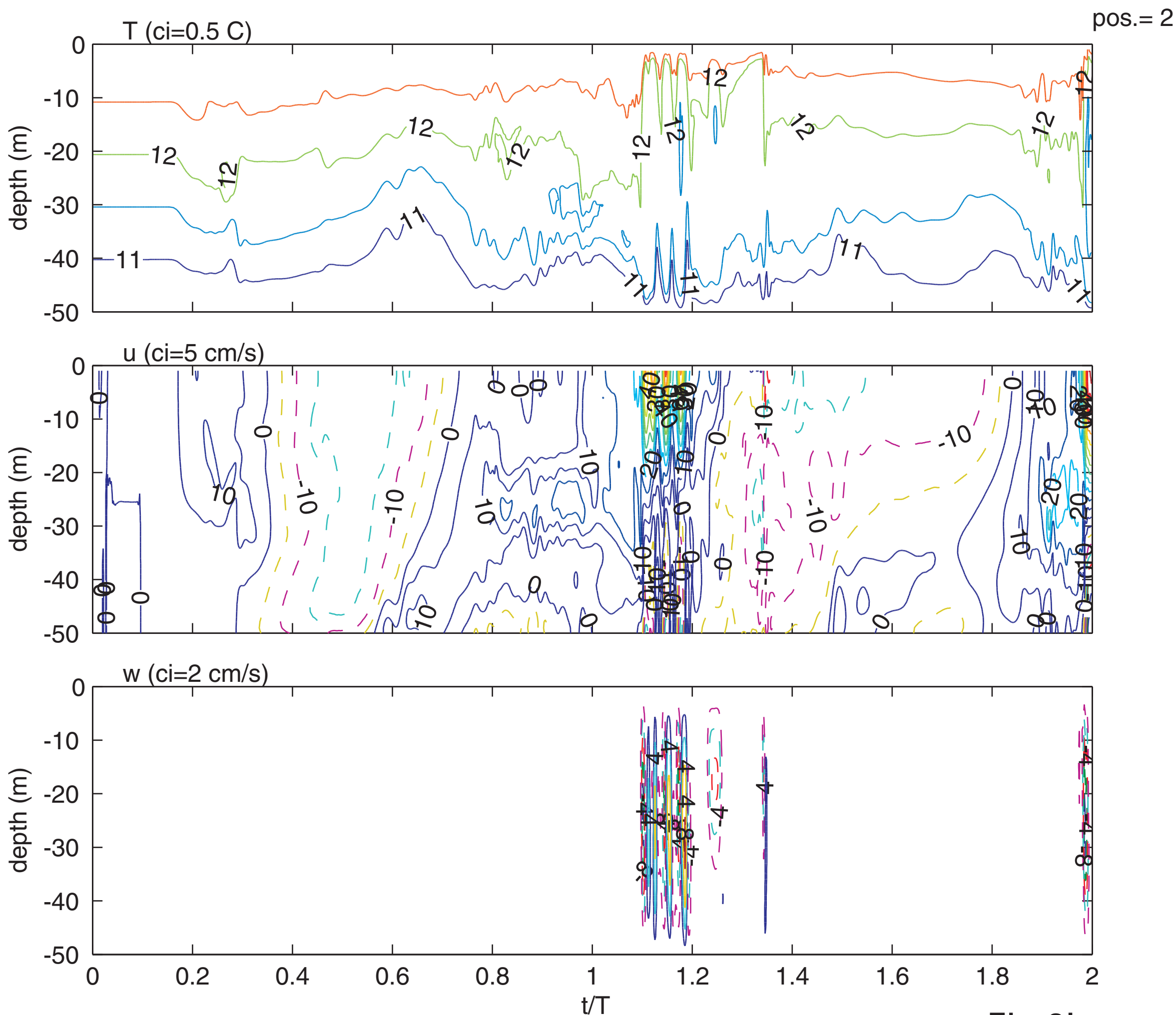
pos.= 2
T (ci=0.5 C)
u (ci=5 cm/s)
w (ci=2 cm/s)
depth (m)
t/T

Fig 9b

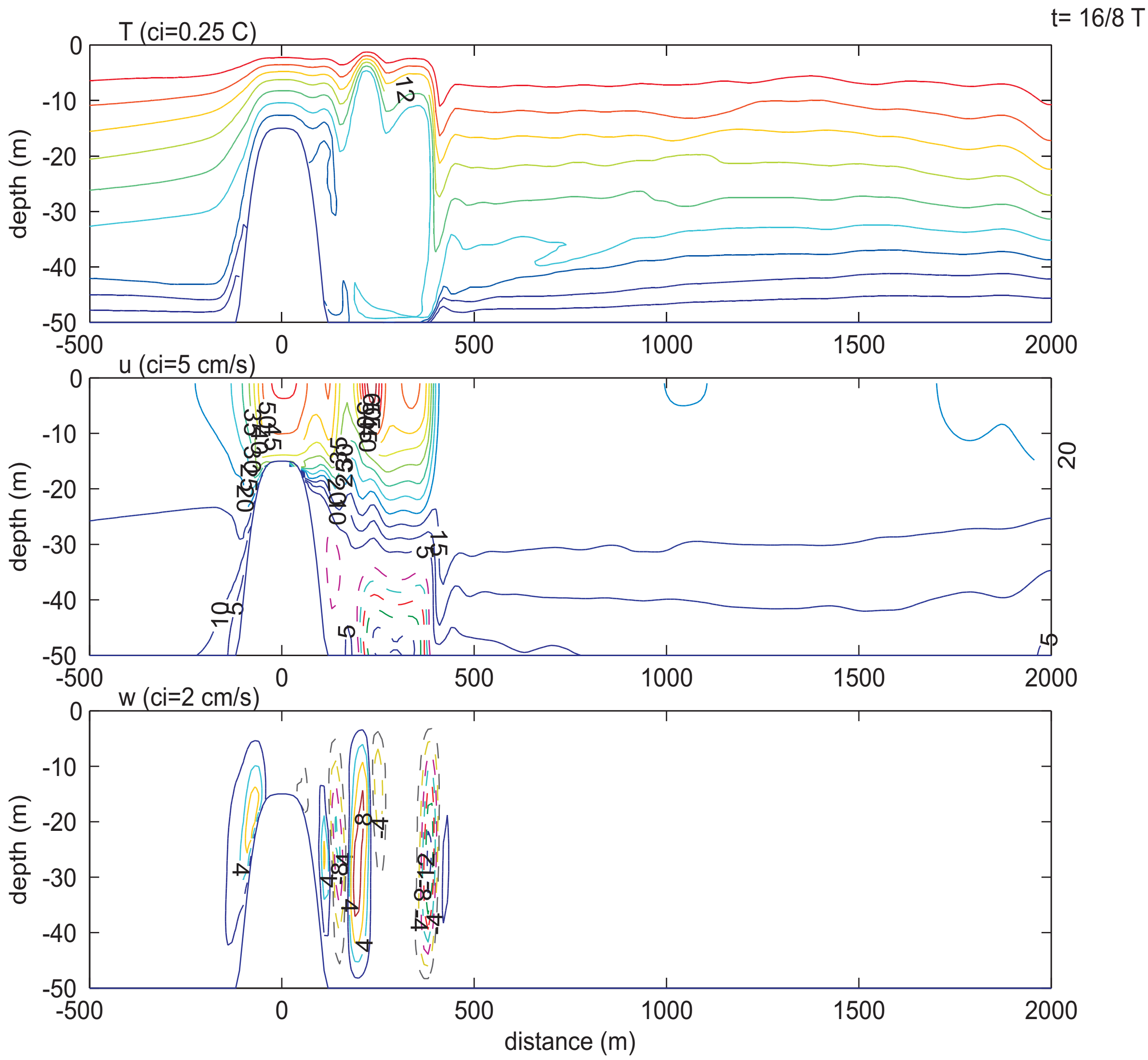

Fig 10a

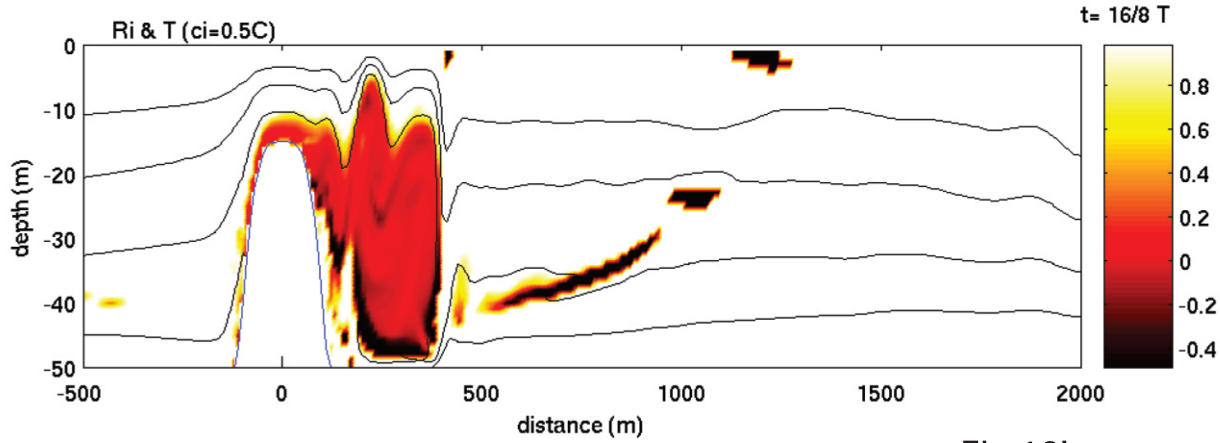

Fig 10b

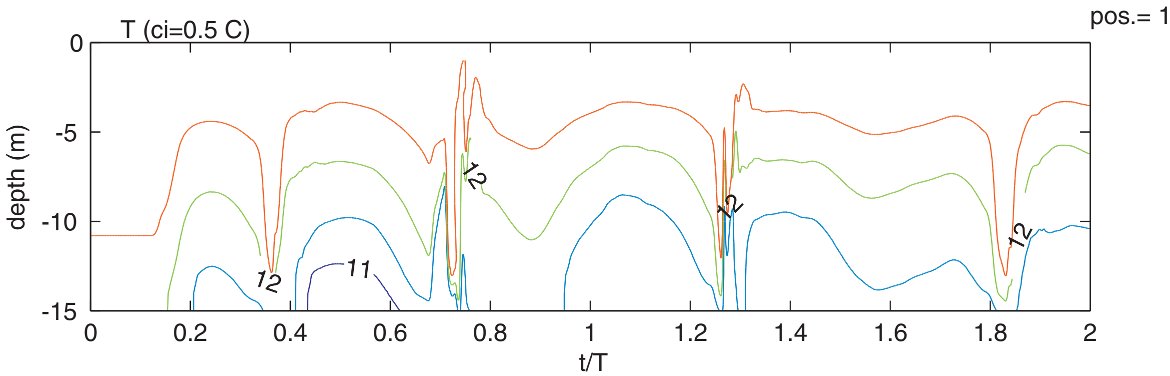
T (ci=0.5 C)
pos.= 1
0
-5
-10
-15
depth (m)
0
0.2
0.4
0.6
0.8
1
1.2
1.4
1.6
1.8
2
t/T
12
11
12
12
12

Fig 10c

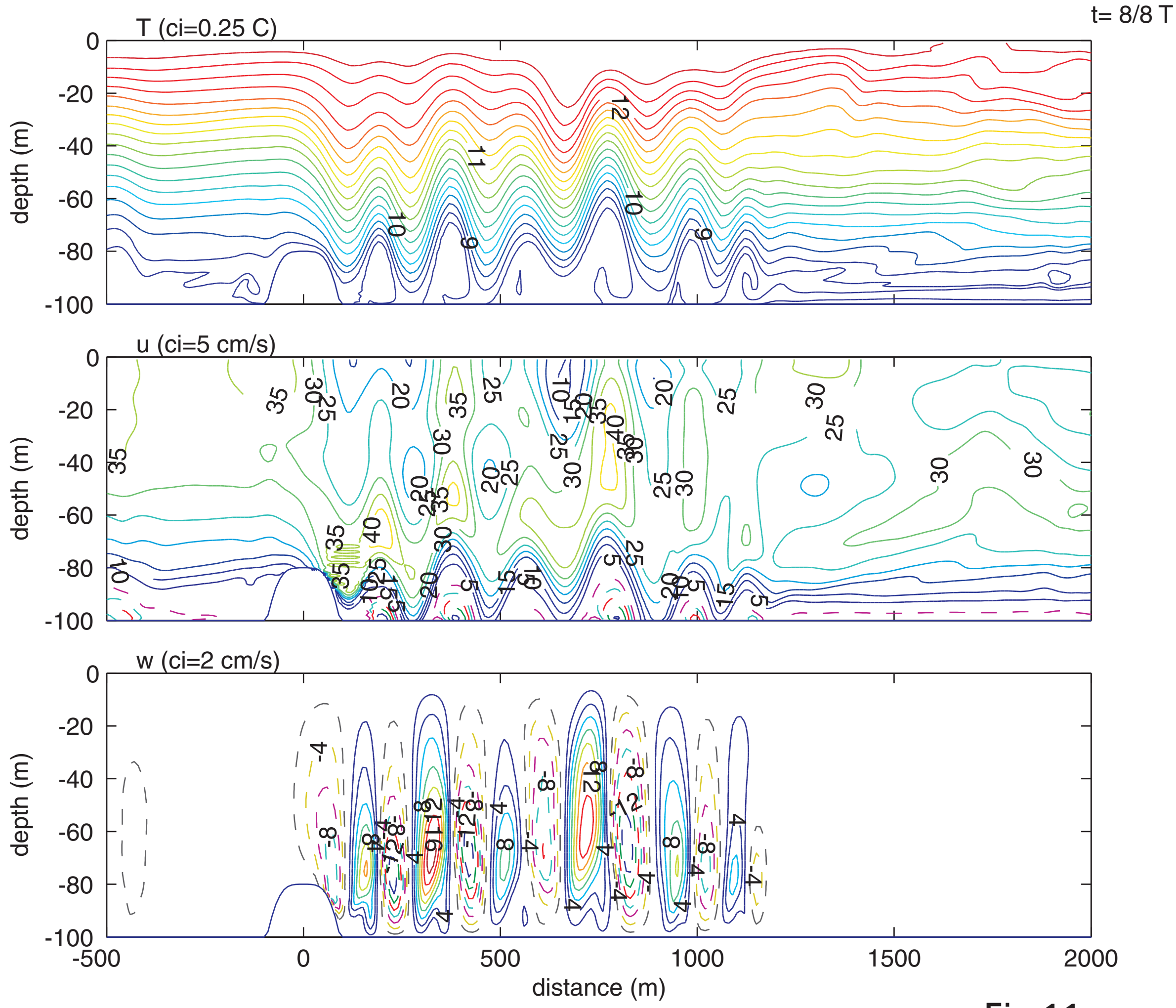

Fig 11a

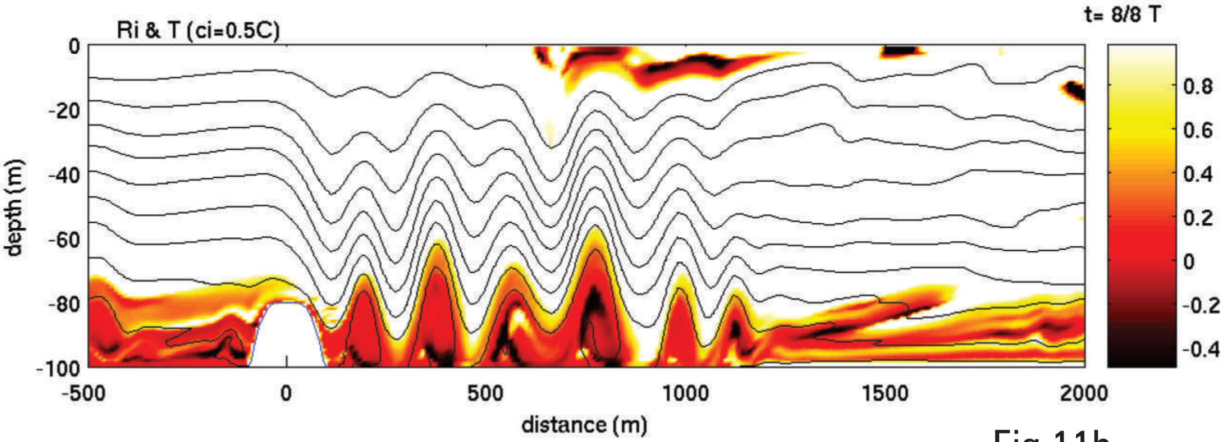
Ri & T (ci=0.5C)
t= 8/8 T
0
-20
-40
-60
-80
-100
depth (m)
-500
0
500
1000
1500
2000
distance (m)
0.8
0.6
0.4
0.2
0
-0.2
-0.4

Fig 11b

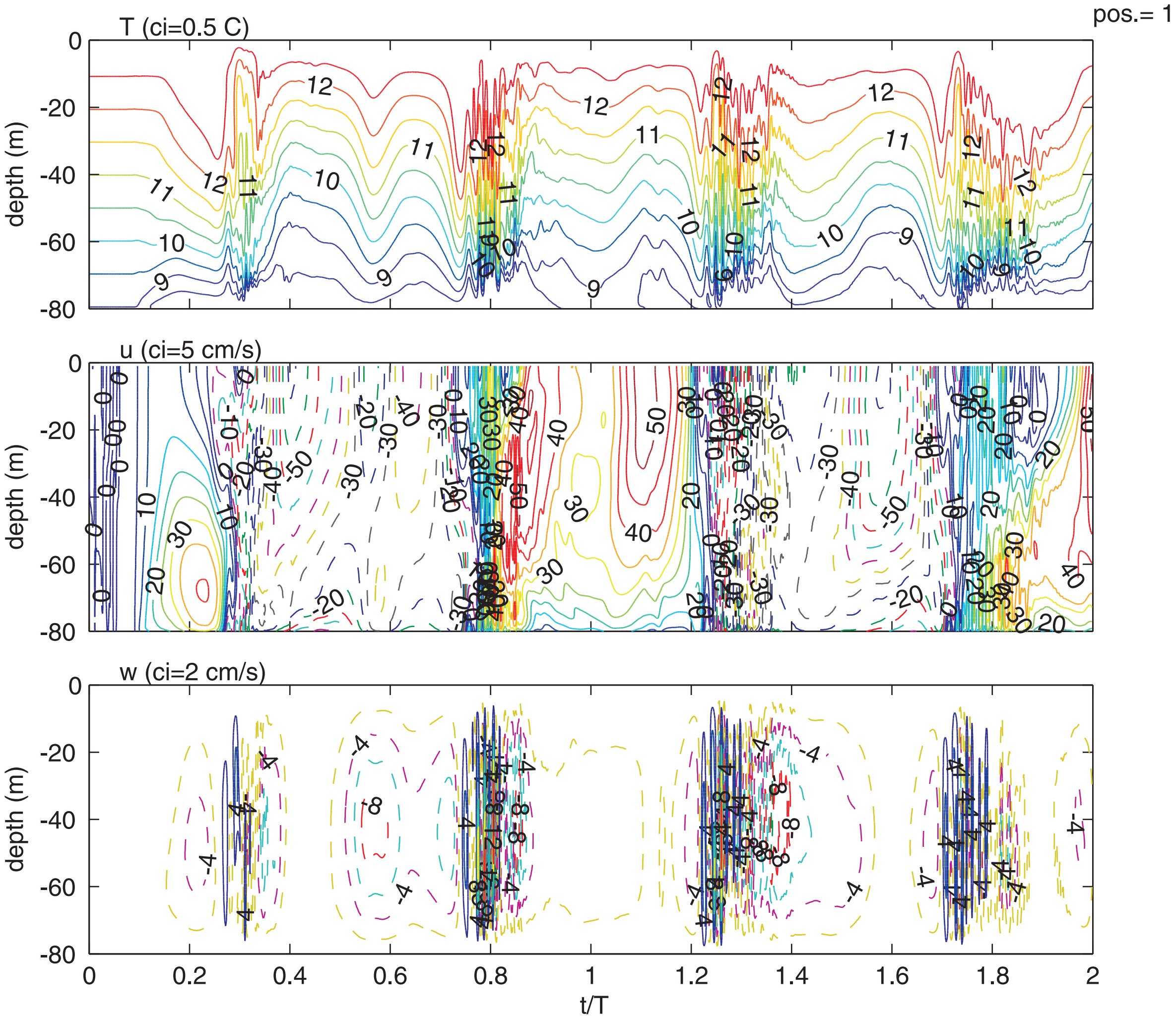

Fig 12

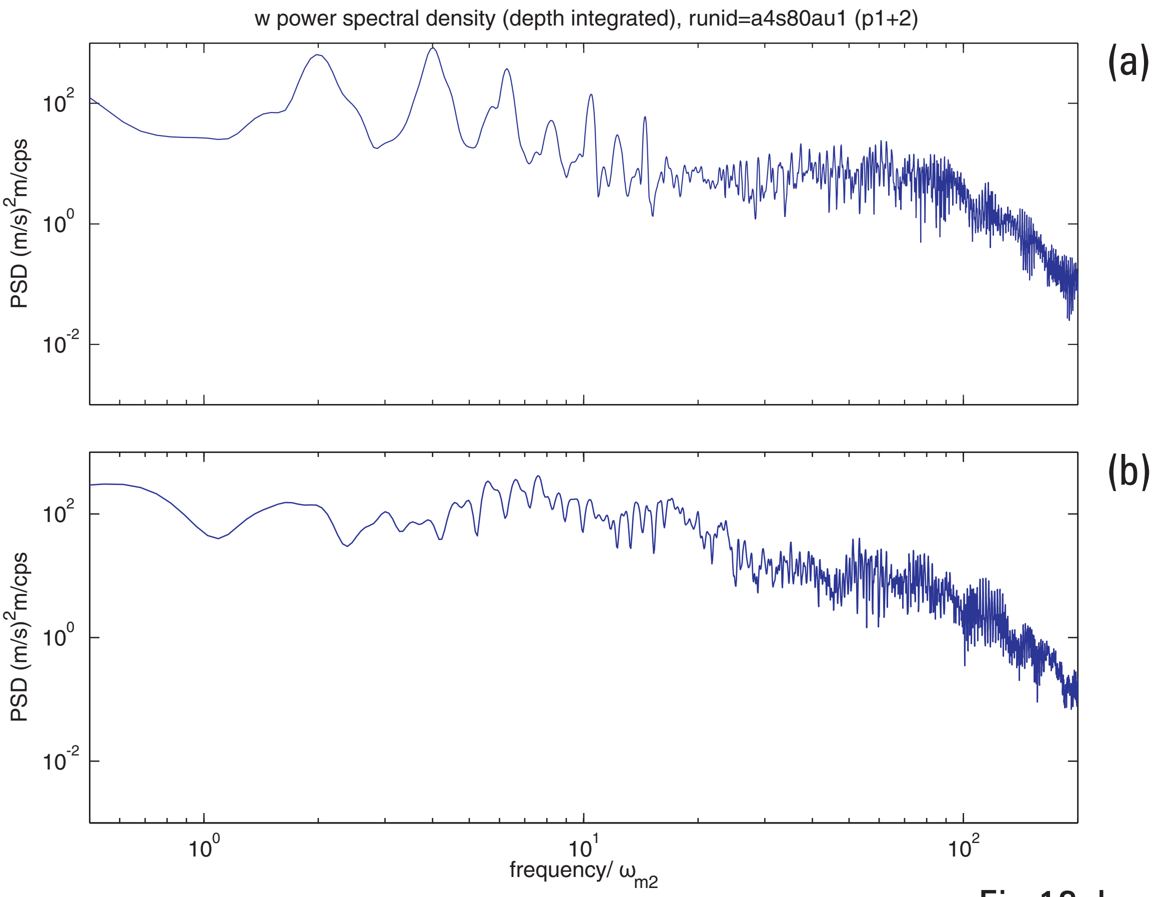

w power spectral density (depth integrated), runid=a4s80au1 (p1+2)
(a)
(b)
PSD (m/s)^{2}m/cps
PSD (m/s)^{2}m/cps
10^2
10^0
10^{-2}
10^0
10^1
10^2
frequency/ ω_{m2}

Fig 13ab